ERRATA

Report No. DOT/FAA/TC-26/13 **Assessment of Emerging Metallic Structures Technologies through Test and Analysis of Fuselage Structure: Test Panel 3**

August 2026

Prepared for

Department of Transportation
Federal Aviation Administration
William J. Hughes Technical Center for Advanced Aerospace
Atlantic City International Airport, NJ 08405

This update addresses the omission of an Author's name and corrects the title. All technical content remains valid and unchanged.

Please replace file tc26-13.pdf, dated 2026-08-18 with the attached file tc22-11.pdf, dated 2026-08-19.

Released August 2026

1 Attachment: tc26-13.pdf

DOT/FAA/TC-26/13

Federal Aviation Administration
William J. Hughes Technical Center
Aviation Research Division
Atlantic City International Airport
New Jersey 08405

Assessment of Emerging Metallic Structures Technologies Through Test and Analysis of Fuselage Structure: Test Panel 3

July 2026

Final report

NOTICE

Technical Report Documentation Page

Form DOT F 1700.7 (8-72) Reproduction of completed page authorized

1. Report No.	2. Government Accession No.	3. Recipient's Catalog No.
DOT/FAA/TC-26/13		

4. Title and Subtitle	5. Report Date
Assessment of Emerging Metallic Structures Technologies through Test and Analysis of Fuselage Structure: Test Panel 3	July 2026
	6. Performing Organization Code ANG-E281
7. Author(s) Yongzhe Tian, Mike Kulak, Kamruz Zaman, Kimberly Maciejewski, Marcelo R. B. Rodrigues, and Carlos E. Chaves	8. Performing Organization Report No.
9. Performing Organization Name and Address William J. Hughes Technical Center Federal Aviation Administration Aviation Research Division Structures and Materials Section Atlantic City International Airport, NJ 08405	10. Work Unit No. (TRAIS) 11. Contract or Grant No.
12. Sponsoring Agency Name and Address U.S. Department of Transportation Federal Aviation Administration FAA Transport Airplane Directorate Airframe/Cabin Safety, ANM-115 1601 Lind Avenue SW Renton, WA 98057	13. Type of Report and Period Covered Final Report 14. Sponsoring Agency Code

15Supplementary Notes

16. Abstract

The Federal Aviation Administration (FAA), in partnership with Arconic, Embraer, and National Institute for Aviation Research (NIAR), is assessing emerging metallic structures technologies (EMST) using the FAA's Full-Scale Aircraft Structural Test Evaluation and Research (FASTER) facility and Structures and Materials Lab. In this collaborative effort, the research team will collect full-scale fuselage panel test data to assess the damage-tolerance (DT) performance of certain EMST fuselage design concepts and compare the results to the DT performance of fuselage structures constructed from conventional aluminum materials that are available today. Several technologies will be considered, including advanced aluminum-lithium (Al-Li) alloys and selective reinforcement of the structure using fiber metal laminates (FMLs). Data from this study will be used to verify improved weight and structural safety performance of the EMST design concepts as compared to fuselage structures built from conventional aluminum materials. The data will also be used to assess the relevance of existing FAA policies (e.g., regulations and guidance materials) and to inform whether safety standards and guidance materials should be created or revised to provide improved safety beyond that afforded by existing airworthiness standards. Results from the third panel test are summarized and compared with panel 1 and panel 2 in this report and will be compared to future tests on panels containing reinforcement using FML to assess the damage-tolerance performance.

17. Key Words	18. Distribution Statement
FASTER, Advanced Technologies, Damage Tolerance, Residual Strength, Finite Element Modeling, Aircraft Fuselage Structure	This document is available to the U.S. public through the National Technical Information Service (NTIS), Springfield, Virginia 22161. This document is also available from the Federal Aviation Administration William J. Hughes Technical Center at actlibrary.tc.faa.gov.

19. Security Classif. (of this report)	20. Security Classif. (of this page)	21. No. of Pages	22. Price
Unclassified	Unclassified	71	

Contents

Figures

Tables

Acronyms

Acronym	Definition
Al-Li	Aluminum-lithium
DIC	Digital Image Correlation
EMST	Emerging Metallic Structures Technologies
FAA	Federal Aviation Administration
FASTER	Full-Scale Aircraft Structure Test Evaluation and Research
FCG	Fatigue Crack Growth
FEA	Finite Element Analysis
FEM	Finite Element Modeling
FML	Fiber Metal Laminate
NIAR	National Institute for Aviation Research
SHM	Structural Health Monitoring
SIF	Stress Intensity Factor
SRM	Structural Repair Manual

Executive summary

In partnership with Arconic and Embraer, the Federal Aviation Administration (FAA) is assessing emerging metallic structures technologies (EMST) using the FAA's Full-Scale Aircraft Structural Test Evaluation and Research (FASTER) facility and Structures and Materials Lab. Full-scale fuselage panel test data will be obtained to assess the damage-tolerance (DT) performance of certain EMST fuselage design concepts located just forward of the wing on the crown of a typical single-aisle aircraft. Results will be compared to the DT performance of fuselage structures constructed from conventional aluminum materials that are available today. Several technologies were considered in the scope of the project, including advanced aluminum-lithium (Al-Li) alloys, next-generation clad aluminum alloy, and selective reinforcement of the structure using fiber metal laminates (FMLs). Data from this study will be used to verify improved weight and structural safety performance of EMST design concepts as compared to fuselage structures built from conventional aluminum materials. The data will also be used to assess the relevance of existing FAA policies (e.g., regulations and guidance materials) and to inform whether safety standards and guidance materials should be created or revised to provide improved safety beyond what is afforded by existing airworthiness standards.

Results from the panel 3 test are summarized in this report. A phased approach was undertaken for panel 3 to study two scenarios simulating damage that represents cracks in the structure: (1) a two-bay crack-like notch in the skin along the circumferential direction, with central stringer severed; and (2) a two-bay crack-like notch in the longitudinal direction, with the central frame severed. During phase 2 testing, two mill-line cracks were introduced to study the detectability of several structural health monitoring (SHM) systems.

The results will be compared to panel 1 and panel 2 and future tests on advanced panels containing FML reinforcement to assess the damage-tolerance performance.

1 Introduction

The aircraft industry is striving to both improve performance and reduce costs in fabrication, operations, and maintenance by introducing advanced materials in conjunction with innovative manufacturing and production technologies. In light of the structural material decision made for the B787 and A350 airframe, and increasing competition from composite materials, the aluminum industry has made significant advancements over the past decade in developing new lightweight alloys and product forms, improved structural concepts, and manufacturing processes aimed at being competitive with composite materials in terms of manufacturing cost and performance. Collectively, these advances fall under the umbrella classification of emerging metallic structures technologies (EMST). Substantial investments have been made to demonstrate the potential to design and build durable and damage-tolerant fuselage and wing structures using EMST, including advanced alloys (Prasad, Gokhale, & Wanhill, 2014; Stonaker, Bakucka, & Freisthler, 2015), bonding and joining methods (Bertoni, Fernandez, & Miyazaki, 2014; Chaves, 2017; Kok, Poston, & Moore, 2011; Schmidt, 2005), and metallic-composite hybrids (Bertoni, Fernandez, & Miyazaki, 2014; Beumler, 2014; Chaves, 2017; Heinimann, et al., 2007; Schmidt, 2005; Silva, et al., 2017). Industry is interested in the use of these material systems due to the following benefits:

- In comparison to conventional alloys:
  - Weight savings due to higher strength-to-weight ratios
  - Improvements in other properties (e.g. fatigue and damage tolerance capabilities) resulting in reduced inspection burden and more efficient design
  - Improvements in corrosion resistance
- In comparison to composites:
  - Reduced supply chain challenges (e.g., flexibility and lead time)
  - Reduced fabrication cost

However, the introduction of a new material or concept in the aerospace industry can be quite challenging. A significant amount of test data at the coupon, substructure, and full-scale level is needed to fully vet and properly assess a new technology and understand potential certification and continued airworthiness issues. This includes the assessment of existing regulations and guidance materials to determine if the FAA needs to revise them or create new safety standards or guidance materials. For these reasons, regulators and industry ideally should work together in preparation for the application and certification of EMST.

In recognizing these challenges, the Federal Aviation Administration (FAA), Arconic, Embraer and the National Institute for Aviation Research (NIAR) are collaborating on a research effort to evaluate the damage tolerance performance of certain EMST fuselage design concepts through full-scale testing and analysis. The goal is to assess and verify that the EMST have improved weight and structural safety performance as compared to fuselage structures built from conventional aluminum materials. Several EMST are being considered, including integral frames, new metallic alloys, and selective reinforcement using fiber metal laminates (FMLs). Fuselage panels with various EMST will be designed, fabricated, and tested in this multi-year effort, as shown in Figure 1. Panels will be tested using the FAAs Full-Scale Aircraft Structural Test Evaluation and Research (FASTER) facility, which was designed for testing fuselage panels and is capable of simulating aircraft service load conditions through synchronous application of mechanical and environmental load conditions, Figure 2 (Tian & Backuckas, 2019).

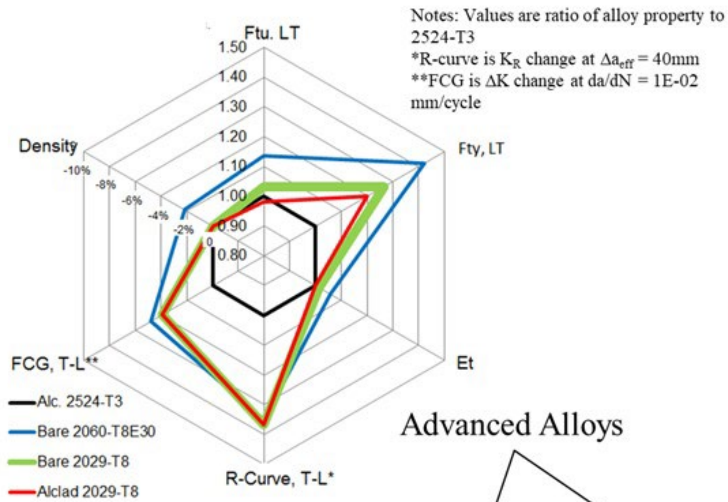

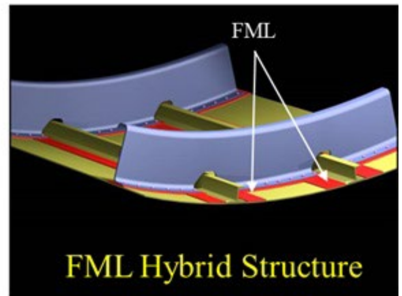

Advanced Alloys

		1 Baseline	2 Advanced Density Reduction	3 Advanced Materials	4 FML Reinforced	5 FML Reinforced (Optimized for Weight)
Component	Skin	2524-T3 sheet	2060-T8E30 Al-Li sheet	2029-T3 sheet	2524-T3 sheet	2524-T3 sheet
Component	Stringer	7150-T77511 extrusions, riveted	2055-T84 Al-Li extrusions, riveted	2055-T84 Al-Li extrusions, riveted	7150-T77511 extrusions, with FML straps	7150-T77511 extrusions, with FML straps
Component	Frame	7075-T62 - shear tied, extruded, riveted	2099-T83 Al-Li integral extrusions , riveted	2099-T83 Al-Li integral extrusions, riveted	7075-T62 - shear tied, extruded with FML straps	7075-T62 - shear tied, extruded with FML straps
Schedule	Start	Oct-17	Jan - 19	June - 21	Sep - 24	July - 26
Schedule	Finish	Dec-18	May -21	Jan - 24	June – 26	Dec - 27

Figure 1. EMST test matrix

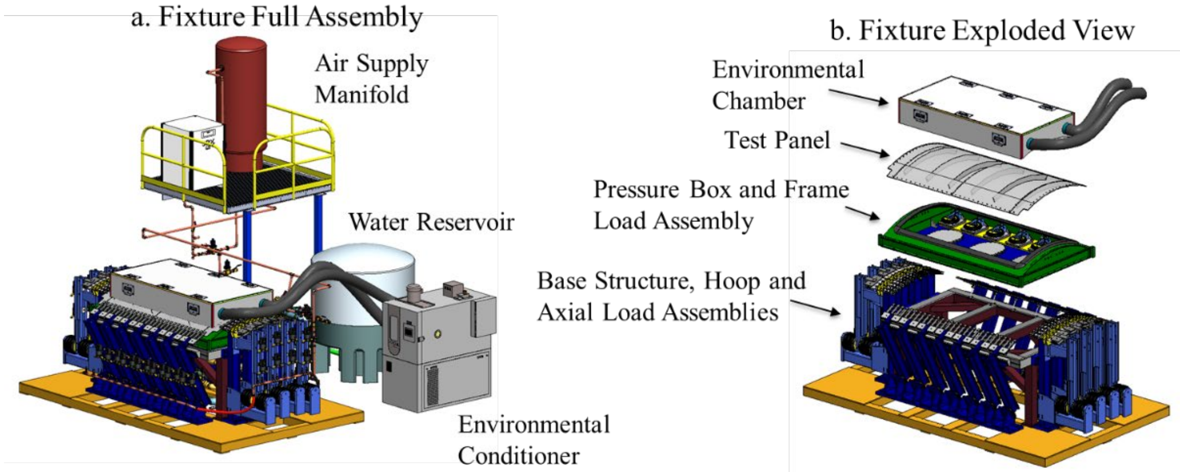

Figure 2. FAA FASTER fixture assembly and major component

A phased approach will be undertaken to study several damage scenarios, including: (1) a two-bay skin crack along the circumferential direction with central stringer severed; and (2) a two-bay skin crack along the longitudinal direction with the central frame severed. For each damage scenario phase, strain surveys will first be conducted and compared to finite element predictions to verify proper load and panel alignment. The panels will then be subjected to fatigue crack growth (FCG) testing using an equivalent constant-amplitude load sequence, determined through coupon-level tests, that represents an effective spectrum loading of a fuselage panel located on the crown of the aircraft, forward of the wing (Kulak, Bakuckas, Tian, & Stanley, 2024; Stonaker, et al., 2019). To demonstrate potential improvements in operational usage when considering aircraft fuselage shells utilizing EMST concepts, an elevated fuselage pressure differential approximately 15% higher than that used in a typical single-aisle transport category aircraft, such as the B737 and A320. The final stage of circumferential crack testing will be a residual strength test to verify limit load conditions identified in 14 CFR 25.571 (Damage-tolerance... , 2023) are met. The final stage of longitudinal crack testing will be a residual strength to failure test to verify limit load conditions are met or exceeded. Data from this program will be used to demonstrate the improvement in damage tolerance and structural safety potential of EMST and provide guidance when considering EMST use.

This report documents results from tests conducted on the third panel, consisting of 2029-T3 skin, 2055-T84 stringers, and 2099-T83 integral frames. Panel 3 was subjected to two phases of testing and accumulated 88,958 simulated flights over a 24-month period. Crack growth was monitored and recorded during all phases of testing using high-magnification cameras, high-frequency eddy current inspection, strain gages, and a digital image correlation (DIC) system. For each phase, prior damage was repaired. Results from panel 3 tests are summarized below and will be compared to baseline panel 1 (Tian, Stanley, & Bakuckas, 2021), panel 2 (Tian, Stanley,

& Bakuckas, 2023), and advanced panels containing varying EMST to assess the damage tolerance performance:

- **Phase 1**: A two-bay crack-like notch in the circumferential direction having a total length (tip-to-tip) of 1.3 in. was machined in the skin with the central stringer severed. The panel was then fatigue-tested under simulated flight load conditions for 46,900 cycles, in which slow and stable crack growth occurred to a final total length of 11.3 in. During the subsequent test conducted up to approximately 2.5 g (g-force) axial limit load, local stable tearing extension occurred from each crack tip. The panel was then repaired.
- **Phase 2**: A two-bay crack-like notch in the longitudinal direction having a total length of 3.25 in. was machined in the skin with the central frame severed and then fatigue-tested to 42,058 cycles. During the fatigue test, the crack grew across two frame bays to a final total length of 12.5 in. The fatigue crack was then extended with a saw cut all the way to the edge of the frame flange to the final crack length of 40 in. Afterwards, a residual strength test was conducted during which the panel failed at an applied pressure of 13.3 psi.

2 Experimental procedure

Testing for this program was conducted using the FAA's FASTER facility. A description of the test panel, test phases, applied loads, inspection, and monitoring methods are outlined in this section.

2.1 Target application and panel description

The target aircraft considered in this study is a typical single-aisle airplane, such as the B737 or A320. The location of the fuselage panel is assumed to be the crown just forward of the wing, where the primary modes where the simplified loading of pressurization and vertical bending due to flight and landing loads represented the relative performance of the EMST panels. LMI Aerospace was contracted by Arconic to fabricate the baseline panel using standard aerospace manufacturing practices, including but not limited to forming, chemical milling, surface treatment, and joining technologies. The test article, panel 3, was fabricated according to drawings provided in Appendix A.

The final panel dimensions were 125 in. × 76 in. with a radius of 74 in., as shown in Figure 3. The skin material was 2029-T3 with a pocketed construction, where the skin thickness was 0.053 in. in the mid-bay regions and 0.065 in. in the pad-up regions under the frames and stringers. Note that the panel was designed to have a pocket skin thickness of 0.055 in. with a build tolerance of 0.005 in. and was discovered later to have an average pocket thickness of 0.053 in. The impact of thickness difference is addressed by Kulak, Bukackas, Tian & Stanley (2024). The substructure included eight stringers made from 2055-T84 extruded in a Z-section with a 7 in. spacing and six 2099-T8 integral frames with a 20 in. spacing. Reinforcing doublers were installed along the outer perimeter of the skin and to the frame ends for load attachment points of the fixture. Holes of 0.5 in. diameter were drilled along the reinforced doubler edge of the panel for load introductions in the axial and hoop directions. Loads were also introduced into each frame. The major panel dimensions are listed in Table 1. The materials used for the major components are listed in Table 2.

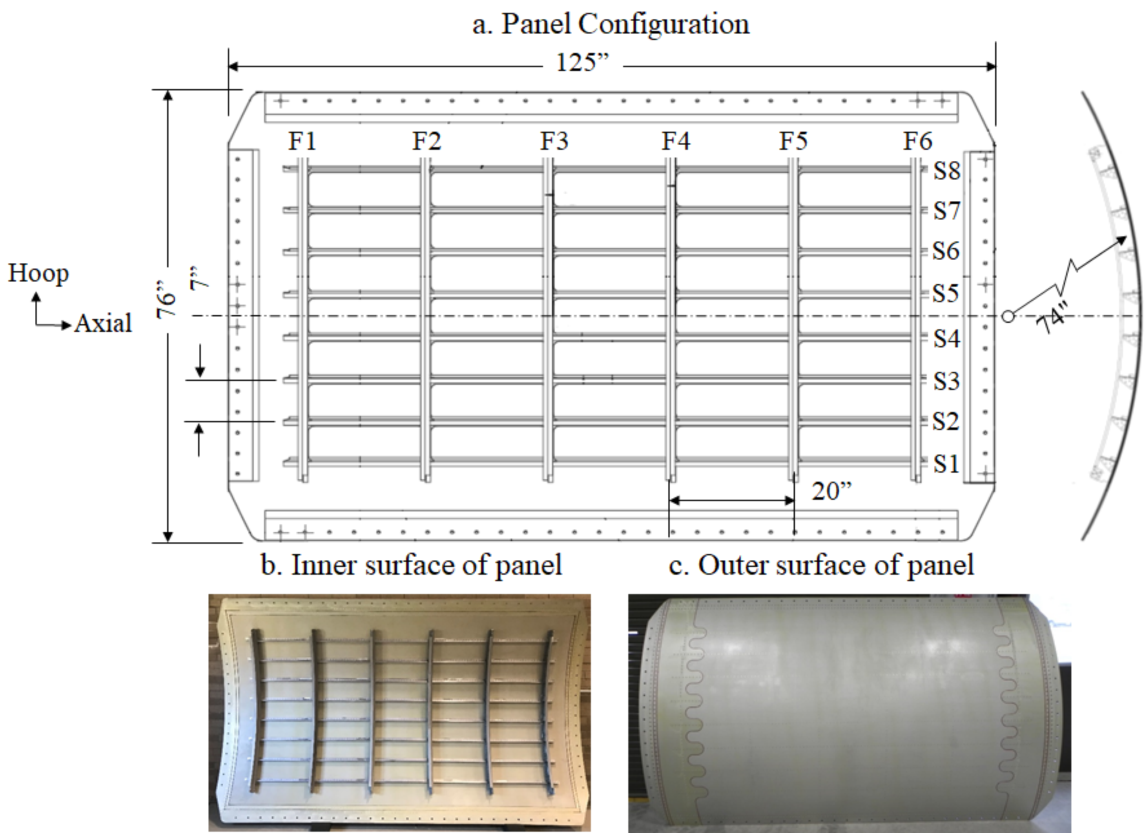

Figure 3. Panel 3 configuration and views of the internal and external surface

Table 1. Panel 3 dimensions

Panel length	125 in.
Panel width	76 in.
Panel radius	74 in.
Panel skin thickness, pad-up	0.065 in.

Panel skin thickness, mid-bay	0.053 in.
Number of frames	6
Number of stringers	8
Frame spacing	20 in.
Stringer spacing	7.0 in.

Table 2. Component materials used to fabricate panel 3

Component	Material
Skin	2029-T3 sheet
Stringer	2055-T84 extrusions, riveted
Frame	2099-T83 extrusions, riveted

2.2 Test phases and damage scenarios

A phased approach was undertaken to study the two damage scenarios, summarized as follows.

Phase 1: Initial damage consisted of a crack-like notch having a length of 1.3 in. in the circumferential direction spanning two skin bays between frames F2 and F3, with the central stringer S4 severed (see Figure 4, Phase 1). The panel was fatigue tested under loads representing pressure, flight maneuver and gust accelerations, and landing loads in the forward crown section of a single-aisle aircraft. Fatigue testing was conducted until the crack extended to a final total length of 11.3 in. Afterwards, a limit load test was conducted, during which the panel was subjected to approximately 2.5 g axial load while holding the pressure constant under operational conditions. The panel was then repaired for follow-on phase 2 (Appendix B).

Phase 2: Initial damage consisted of a two-bay longitudinal crack-like notch between stringers S6 and S7, with the central frame/shear tie F4 severed, as shown in Figure 4, Phase 2. A 3.25 in. long notch was inserted with the underneath frame severed. Initial strain surveys and finite element analysis (FEA) were conducted to ensure proper load introduction and to verify no effects from the repairs made in Phase 1. The panel was then fatigue tested, simulating pressure-only operational conditions, until the crack extended to a final length of approximately 12.5 in. The 12.5 in. crack was extended manually to 40 in. A residual strength test was finally conducted to failure, measuring the load-carrying capacity of the panel.

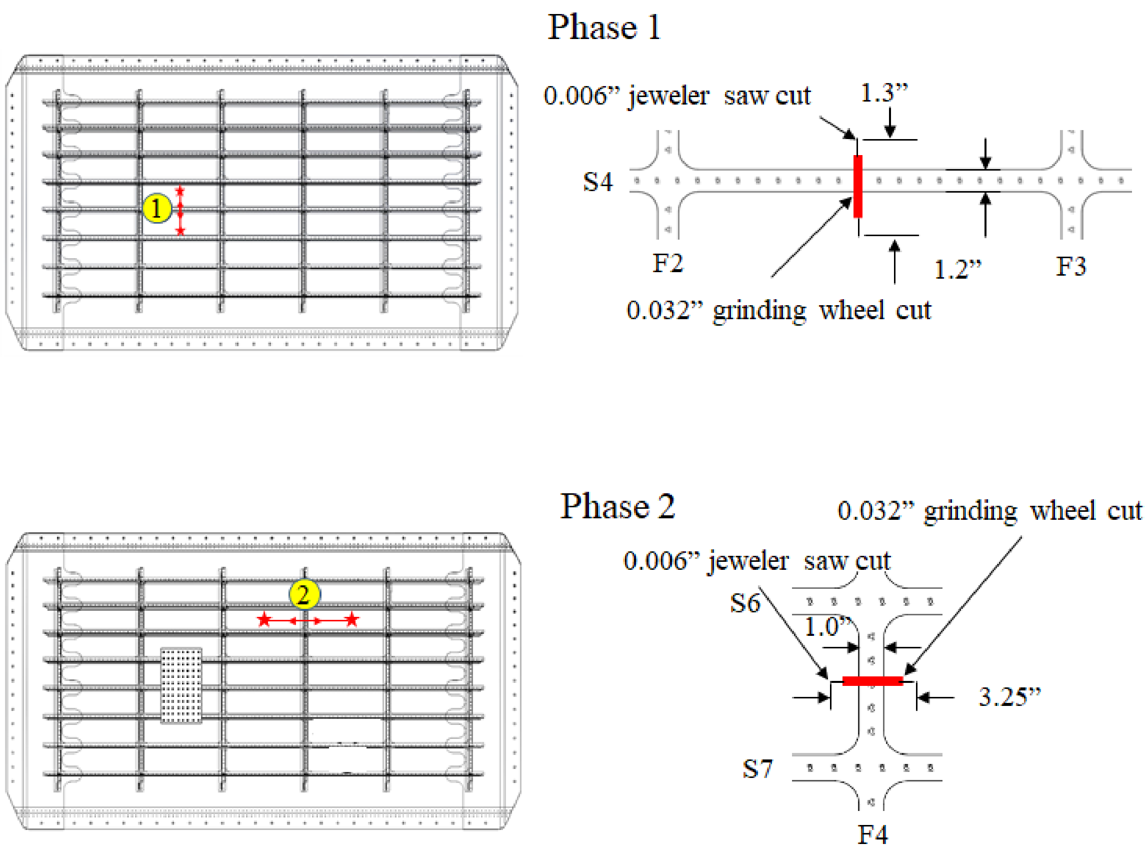

Figure 4. Initial damage scenarios used in the two test phases

2.3 Inspection and monitoring methods

During all phases of testing, several nondestructive inspection methods were used to monitor and record the formation and growth of cracks. Visual inspections were made on the inner and outer surfaces of the skin using high-magnification cameras that could be remotely controlled during the test. High-frequency eddy current was used on the outer surface of the skin. Along with these inspection methods, the baseline panel was instrumented with approximately 120 strain gages and digital image correlation DIC systems to monitor strains throughout the tests, as summarized in Appendices C and D, respectively. In addition, a commercial piezoelectric-based structural health monitoring system was used to collect data and to assess its capabilities to monitor FCG, highlighted in Appendix E.

2.4 Applied mechanical loads

The original goal of this program was to test different EMST fuselage panels under the same loading conditions at a location in the crown of a single-aisle commercial aircraft, where the loads are primarily due to pressure and bending from flight and landing loads. At this location, the damage tolerance performance was the key design criterion for skin/stiffening element sizing in both the longitudinal and circumferential directions. However, the panel 3 skin thickness in the pocketed regions was delivered approximately 10% thinner than panel 1 due to small manufacturing tolerance differences in the chem-milling. This would have resulted in a significant difference in crack growth life using the same load conditions. The skin thickness difference in the "as-built" panel 3 was accounted for by testing panel 3 to the same stress intensity factors versus skin crack size as in panel 1 and panel 2 based on finite element modeling (FEM). The FASTER test loads were adjusted using the FEM model results to match the stress intensity factor of panel 1 and panel 2 in order to have an "apples-to-apples" comparison of results between different panels.

3 Finite element analysis

FEA for this program was originally conducted by Arconic, and the models were later transferred to the FAA.

For the Phase 1 circumferential crack, the pressure in panel 3 was kept the same as panel 1 (9.9 psi). The axial loads were determined using the FE panel 3 model. In panel 1 the axial distribution of applied nodal loads along the front and rear edges of panel 1 were not constant because of the stiffer doubler overlapped corners of the panel. A similar trend occurs for the hoop nodal loads along the hoop edges of the panel. For the axial loads on panel 3, this non-constant panel 1 distribution was scaled. The non-constant distribution of the total applied hoop loads along the edges of panel 1 were kept the same in panel 3 as panel 1 because the same pressure was applied. However, at every FE panel 3 hoop load location along the hoop edges the skin component and frame component of the total load was adjusted to reflect the change in skin to stiffening ratio in panel 3 versus panel 1 using the Flugge equations (Flugge, 1952). Although the Flugge equations are approximate while the FE captures the 3D effects, since the total hoop load at each load point along the longitudinal edges of panel 3 was kept the same as panel 1, any small errors in the ratios of applied skin and stiffener loads would be redistributed to reflect the actual three-dimensional FE distribution a few frame thicknesses into the panel. The axial loads were adjusted by trial and error to match the circumferential crack stress intensity factors between panels 1 and 3, as shown in Figure 5. Panel 3 Phase 1 test loads are given in Figure 6 and Figure 7. This approach described above for panel 3 load development (also used for panel 2) was used for two reasons. First, the development of the FE model load equilibrium boundary conditions reflecting conditions in the FASTER fixture are complex. That is, in FASTER the panel loads are in equilibrium. Any mismatches are equilibrated by the radial links at the frame ends constraining against radial movement. These links are designed to be a safety feature, restraining panel movement during residual strength failure under pressure loading. The goal is to minimize loads in the radial links, which is a measure of equilibrium of the applied FASTER loads. The second main reason for the approach taken involves the heavy doubler system needed to introduce loads around the edges of the panel, which impacts the distribution of applied loads (i.e. load varies from mid edge to panel corner). These doublers also require extra loads that are not in the fuselage. These extra loads are needed to stretch the doublers to match boundary conditions of the panels in the fuselage. Details of the approaches used to develop test loads in panel 1 are provided by Kulak et al. (2024).

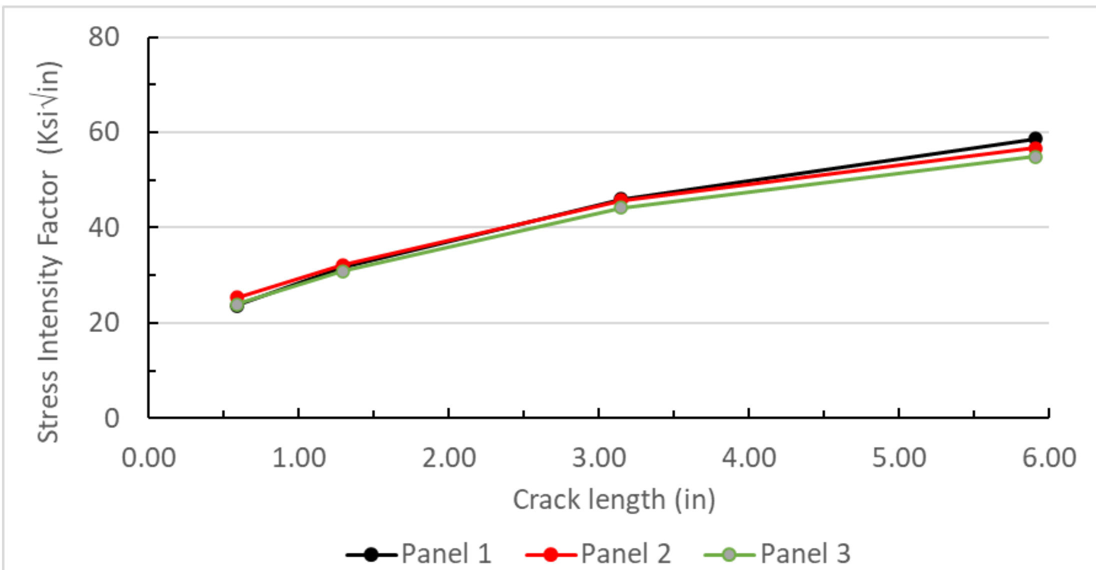

Figure 5. Phase 1 stress intensity factor comparison between panels 1-3

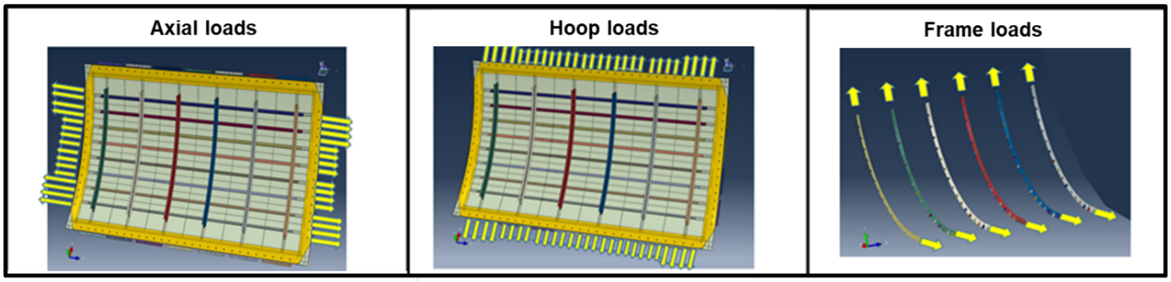

Skin Axial Actuator Load Arm Number	Applied Load (lbf)
1-4	18,851
5-8	11,825
9-12	11,825
13-16	18,851

Skin Hoop Actuator Load Arm Number	Applied Load (lbf)
1-4	10,428
5-8	9,715
9-12	9,491
13-16	9,402
17-20	9,491
21-24	9,715
25-28	10,428

Frame Number	Applied Load (lbf)
1	2,002
2	2,717
3	2,731
4	2,731
5	2,717
6	2,002

Figure 6. FASTER actuator loads for panel 3 Phase 1 fatigue test

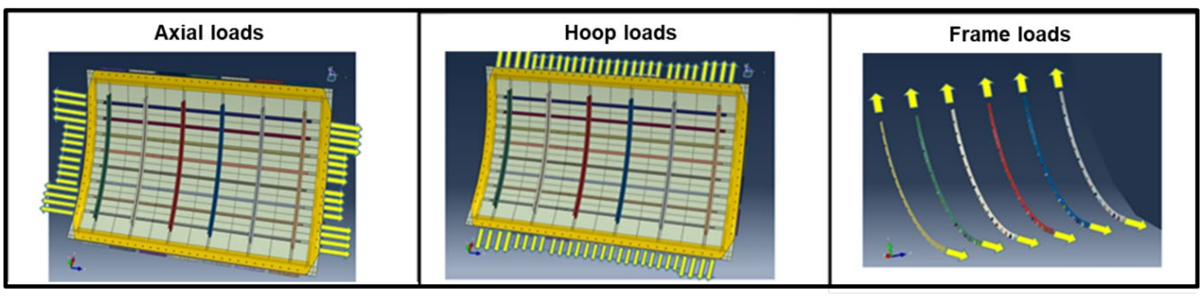

Skin Axial Actuator Load Arm Number	Applied Load (lbf)
1-4	36,516
5-8	22,823
9-12	22,823
13-16	36,516

Skin Hoop Actuator Load Arm Number	Applied Load (lbf)
1-4	10,428
5-8	9,715
9-12	9,491
13-16	9,402
17-20	9,491
21-24	9,715
25-28	10,428

Frame Number	Applied Load (lbf)
1	2,002
2	2,717
3	2,731
4	2,731
5	2,717
6	2,002

Figure 7. FASTER fixture actuator loads for Phase 3 limit load

Phase 2 fatigue loads were determined by matching the panel 3 stress intensity factors to panel 1 as-tested stress intensity factors. The same approach described above was used for the longitudinal crack load development. In this case, the axial load distribution due to pressure was also scaled (no bending loads were used for the longitudinal crack case). In addition, pressure was adjusted until the longitudinal crack stress intensity factor (SIF) solutions matched those in panel 1. Thus, in the hoop direction the total panel 1 hoop loads at every load location changed in proportion to the pressure change, while the components of skin versus frame loads were determined as before using the Flugge equations (Flugge, 1952). Pressure was adjusted by trial and error to 8.64 psi to produce the best match to the panel 1 stress intensity factors. The axial loads used for the Phase 2 fatigue-crack growth test are shown in Figure 8.

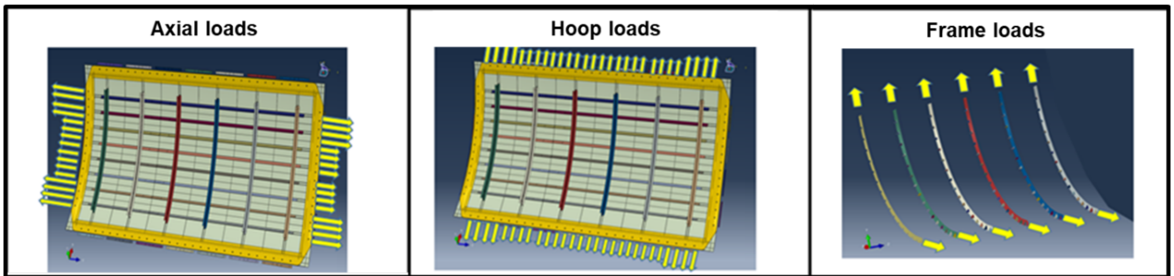

Skin Axial Actuator Load Arm Number	Applied Load (lbf)
1-4	6,794
5-8	4,246
9-12	4,246
13-16	6,794

Skin Hoop Actuator Load Arm Number	Applied Load (lbf)
1-4	9,100
5-8	8,479
9-12	8,284
13-16	8,205
17-20	8,284
21-24	8,479
25-28	9,100

Frame Number	Applied Load (lbf)
1	1,747
2	2,371
3	2,384
4	2,384
5	2,371
6	1,747

Figure 8. FASTER fixture actuator loads for Phase 3 fatigue test, pressure only

4 Results and discussion

Tests and analyses were performed to determine the damage-tolerance performance of panel 3. The results from panel 3 will be used for comparison to panel 1, panel 2 and future advanced fuselage panels with varying EMST. Representative results focus on panel 3 test for each phase.

4.1 Phase 1: two-bay circumferential notch with central stringer severed

4.1.1 Initial strain survey

A central crack-like notch was machined in the skin above the severed stringer S4, which is 1.30 in. long and 0.032 in. wide. The notch was centered about the removed fastener; the geometry is shown in Figure 9. Initial strain surveys were conducted to verify proper load introduction to the baseline panel and validate the FEA model.

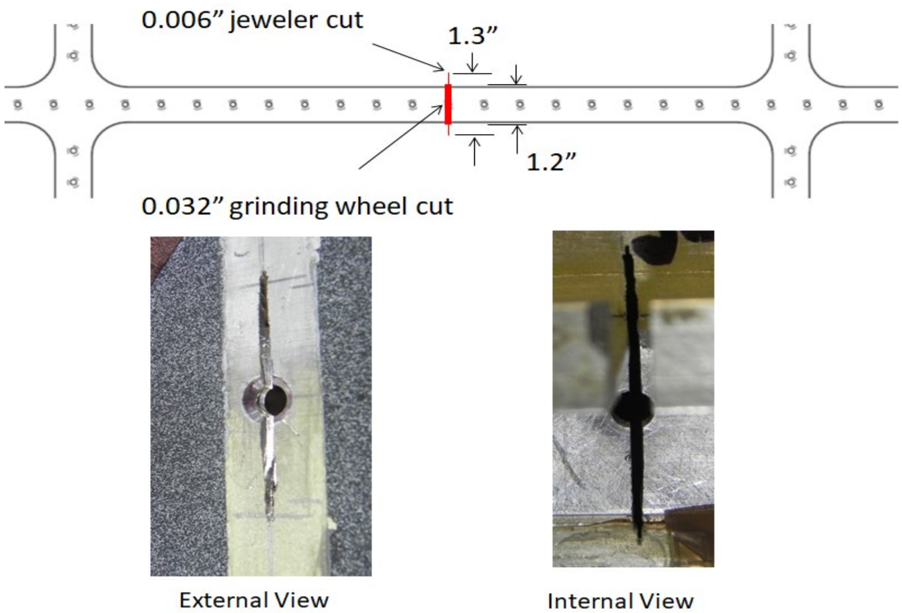

Figure 9. Configure of Phase 1 damage scenario

Figure 10. Phase 1 strain survey results verify FEA and applied

4.1.2 Fatigue test

The panel was fatigue tested under simulated flight load conditions for 48,850 cycles, during which the skin crack extended across two stringer bays to a final length of approximately 11 in., as shown in Figure 11 and Figure 12. In general, slow and stable crack growth was observed during the fatigue test. The crack surface morphology had distinct transition points where, on both sides, the crack surfaces changed from flat to S (slant) fracture. Results indicate that crack-growth rates changed at these transition points similar to those observed in panel 1 and panel 2 testing (Tian, Stanley, & Bakuckas, 2021).

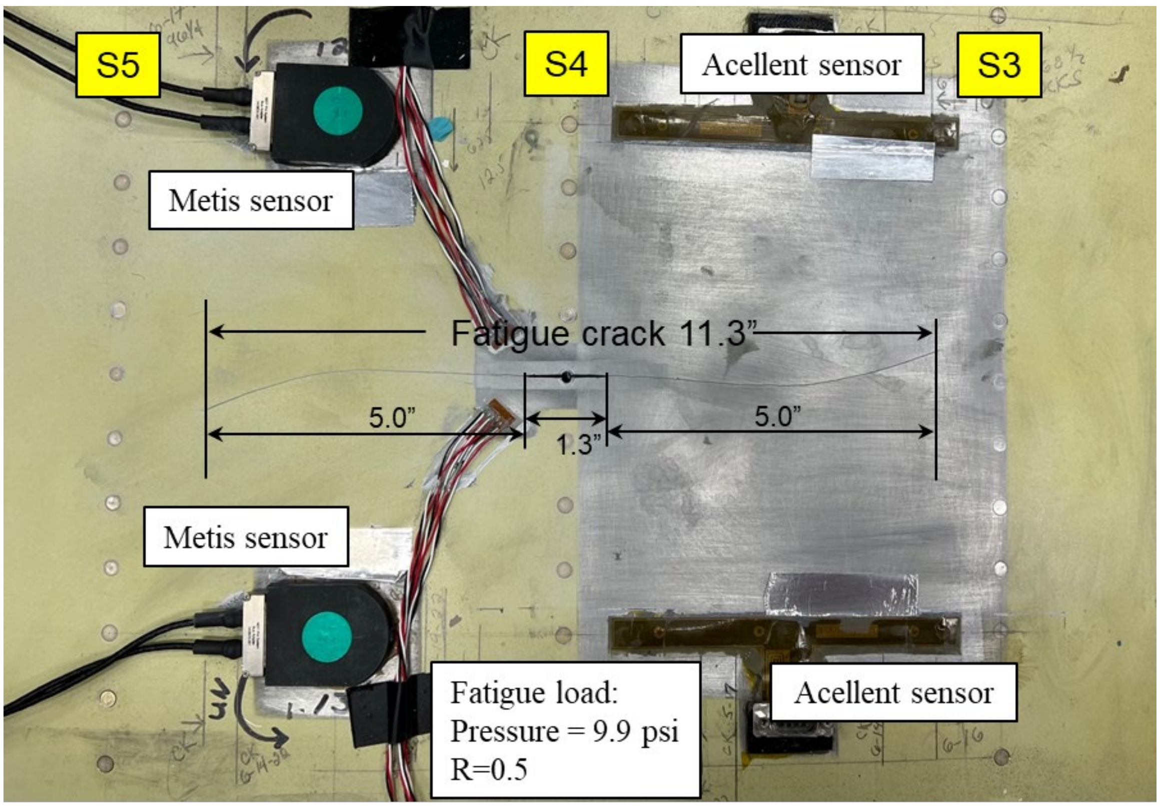

Figure 11. Picture of Phase 1 fatigue crack growth at 48,850 cycles

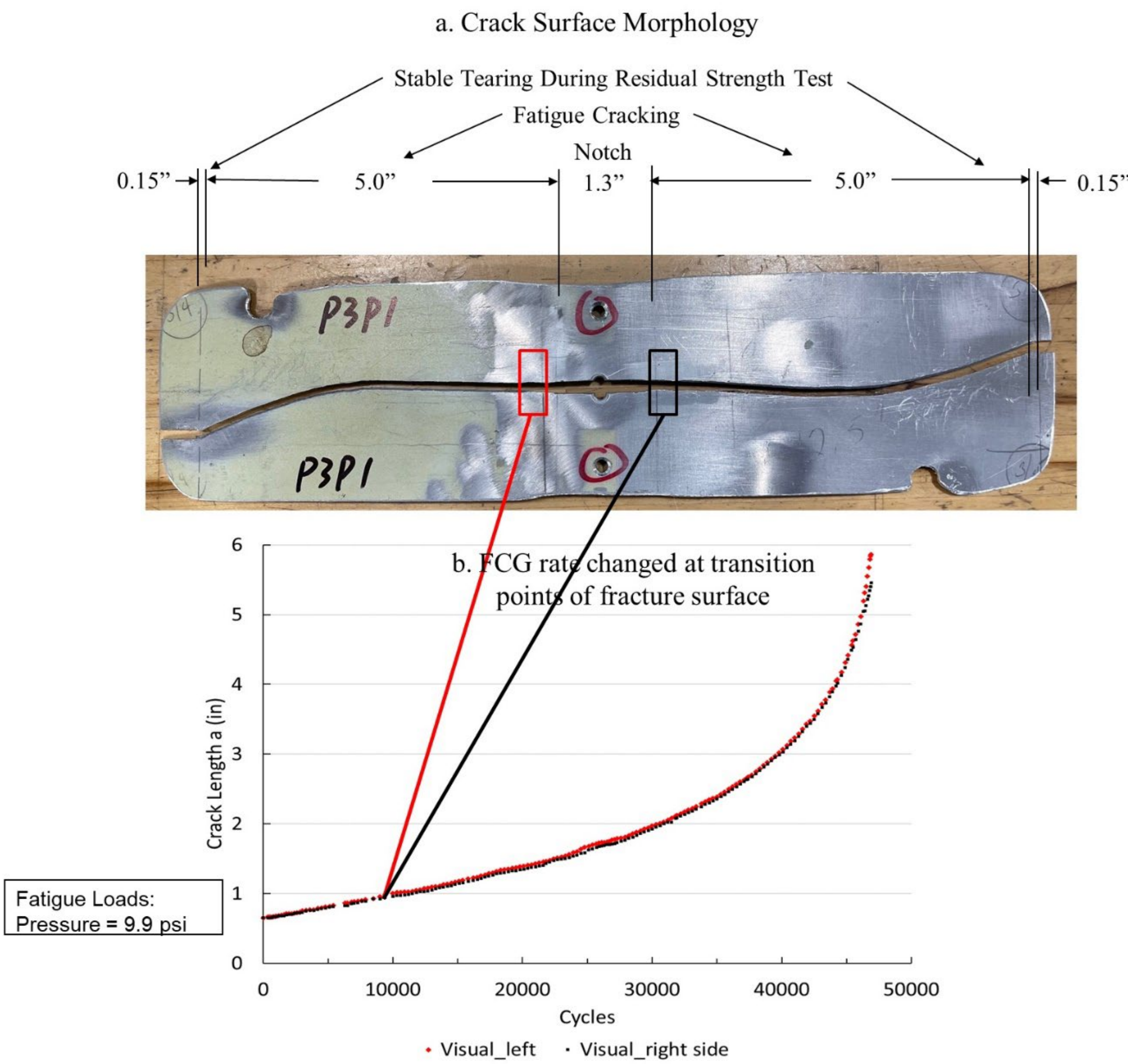

Figure 12. Phase 1 transition points of fracture surface morphology where FCG rates change

As shown in Figure 13, panel 3 exhibited better fatigue crack growth performance compared to panel 1. Crack extension occurred across two stringer bays to a final length of about 11 inches after 33,600, 48,850 and 46900 fatigue cycles in panel 1, 2 and 3, respectively.

Strain surveys were conducted during the fatigue test at same crack length as panel 1 (panel 1 strain survey was conducted at 3000 cycle intervals). The far-field strains in the mid-bay regions remained relatively constant throughout the fatigue test. Slight strain redistribution was evident after 30,000 cycles due to the crack extension, as shown in Figure 14. Strains increased in gages 7 and 10, as the crack grew closer to those gages. In addition, strains in gage 8 reduced due to crack shielding.

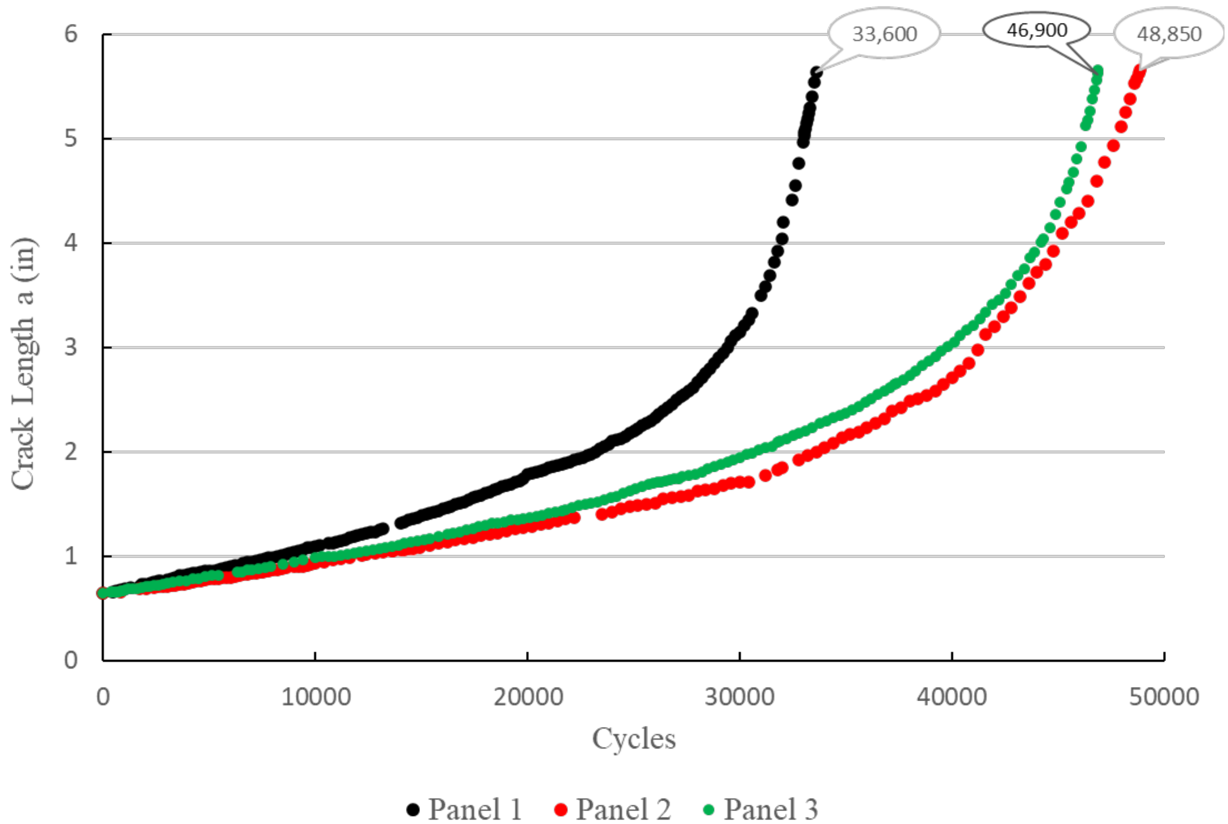

Figure 13. Circumferential crack growth comparison between panels 1, 2, and 3

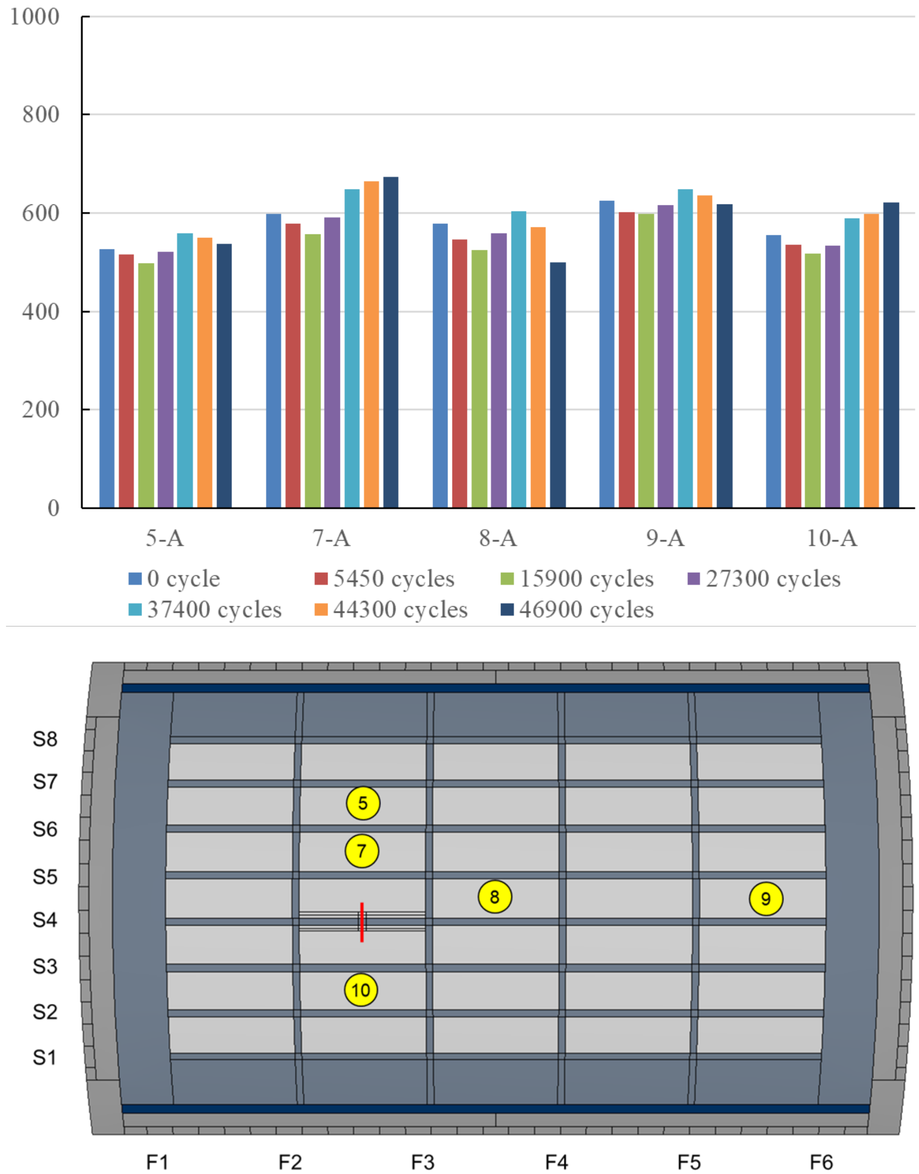

Figure 14. Far-field axial strain distribution measured in skin mid-bay regions during the fatigue test

Local to the crack, strain redistribution was more significant on internal local skin and stringer gages, as shown in Figure 15 and Figure 16, respectively. The magnitude of strain increased as the crack tip approached the gages. As the crack grew past the gages, strains in the skin subsequently reduced.

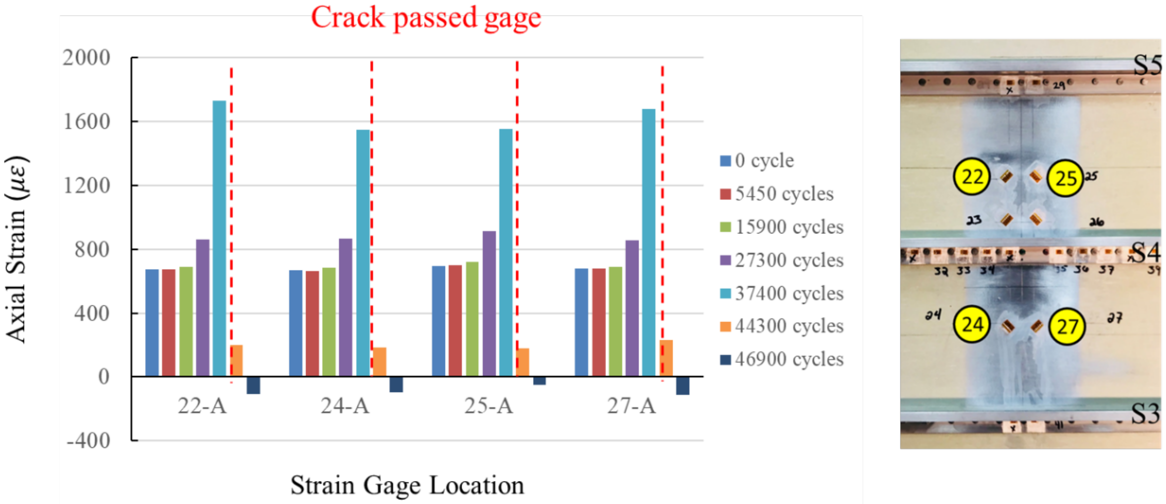

Figure 15. Representative strain survey results for Phase 1 internal skin rosette gages

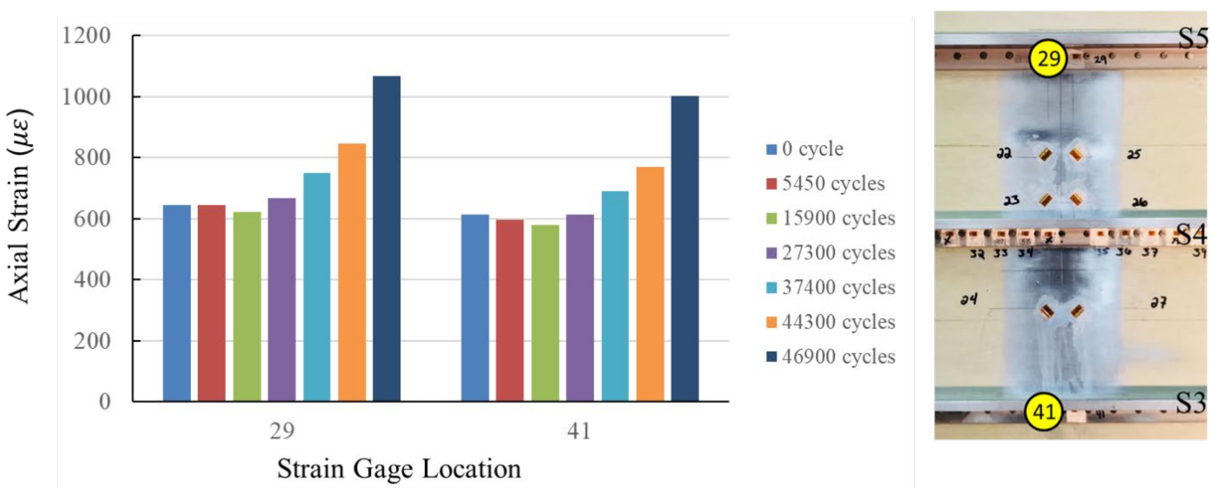

Figure 16. Representative strain survey results for Phase 1 stringer gages

4.1.3 Limit load test

After fatigue testing, panel 3 was subjected to axial direction limit load testing, holding the pressure constant at 9.9 psi. Determining circumferential crack limit loads for all panels was complicated, because the final "as built" average skin thicknesses varied among panels 1, 2, and 3. The approach is described below.

For the circumferential crack, the thicker skin "as built" panel 1 was loaded in constant amplitude at a target equivalent constant amplitude axial target working stress of 13 ksi (translates to 12.7 ksi at 1G+pressure mean flight stress (MFS) for spectrum loading) established by K-Control spectrum and K-Control constant amplitude supplemental testing conducted using the thinner “as designed” panel 1 skin (0.055 in. skin thickness in the pocket area). This thicker 0.059 in. skin issue was not discovered until after panel 1 testing. In other words, the thicker 0.059 in. “as built” panel 1 was inadvertently tested in FASTER to a smaller effective axial crack growth load, and therefore, a smaller axial limit load than those for a 0.059 in. skin “as built” panel 1. A consistent way to develop limit loads for the “as built” 0.059 in. panel 1 would involve the same panel sizing approach used for the “as designed” panel 1 (Kulak, Bakuckas, Tian, & Stanley, 2024). In this new sizing study, the crack growth and limit loads when the skin thickness in the pockets is 0.059 in. would be used for the panel 1 FASTER testing.

Panel 2 was built to a skin thickness of 0.050 in. in the pocketed regions versus the “as designed thickness of 0.055 in. so similar corrections to the panel 2 limit loads were required (recall crack growth loads for panel 2 were calculated based on matching the SIF solution of panel 1 which involves a completely different set of calculations). An additional correction was included because the target working axial crack growth stress was assumed to be 10% higher than the baseline 2524-T3. That is, for the circumferential crack repeat inspection a target skin stress goal of 14.0 ksi skin stress was assumed versus 12.7 ksi for 2524-T3 when applied at the spectrum 1G+pressure conditions. Note, this improvement was estimated by comparing the differences in constant amplitude Da/Dn crack growth testing and further reduction by a factor for conservatism. Ideally, a better indicator of the target working stresses would be developed using K-Control testing. Changes in crack growth and panel skin thickness are included by resizing panel 2 using the same sizing approach described by Kulak (2024). This approach is to first establish the location for the “as built” panel 2 or 3 geometry in the crown using the sizing approach, and then establish limit loads at this new panel crown location as 2.5*1G,axial stress + 1.0*pressure stress from this study. Once these loads were established, factors to scale panel 1 loads could be developed. Panel 1 FASTER loads are scaled to establish panel 2 loads, because panel 1 loads already include the effect of the heavy edge and corner doubler reinforcements creating non-linear FASTER applied loads along each edge from corner to corner; see discussion and calculations for these new loads for panels 1 and 2 in Kulak, Bukackas, Tian, & Stanley (2024). Extra loads are also included in the panel 1 loads to stretch these doublers and are accounted for in the scaling factors. For panel 3, no correction was made to improved crack growth in the resizing study. Although previous testing showed constant amplitude crack growth was better in 2029-T3 than 2524-T3, limited spectrum crack growth testing showed little improvement. The same approach for limit load was used as described above.

Strain gages located on the inner and outer flanges of the stringer ahead of the fatigue crack revealed that the stresses were below the yield strength of the stringer material (see Figure 17). The intact stringers ahead of the crack were effective in containing the damage. In addition, limited stable-tearing extension and crack tip plasticity were observed from each crack tip, as shown in Figure 18 using DIC measurements.

The panel was then repaired for follow-on phases, as shown in Appendix B. The strain survey was conducted to ensure there was no effect of repair on Phase 2 test bay, as shown in Figure 19.

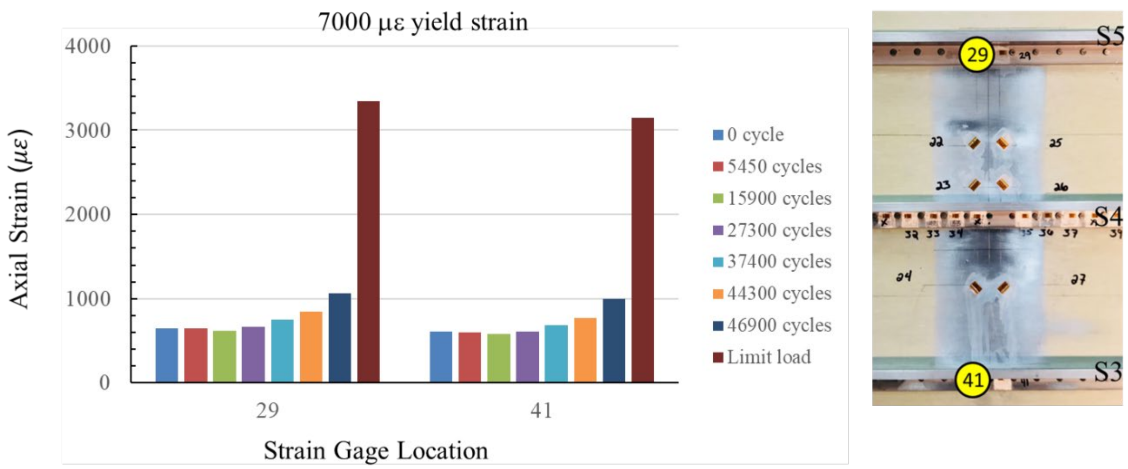

Figure 17. The result of stringer gages during the circumferential direction limit load test

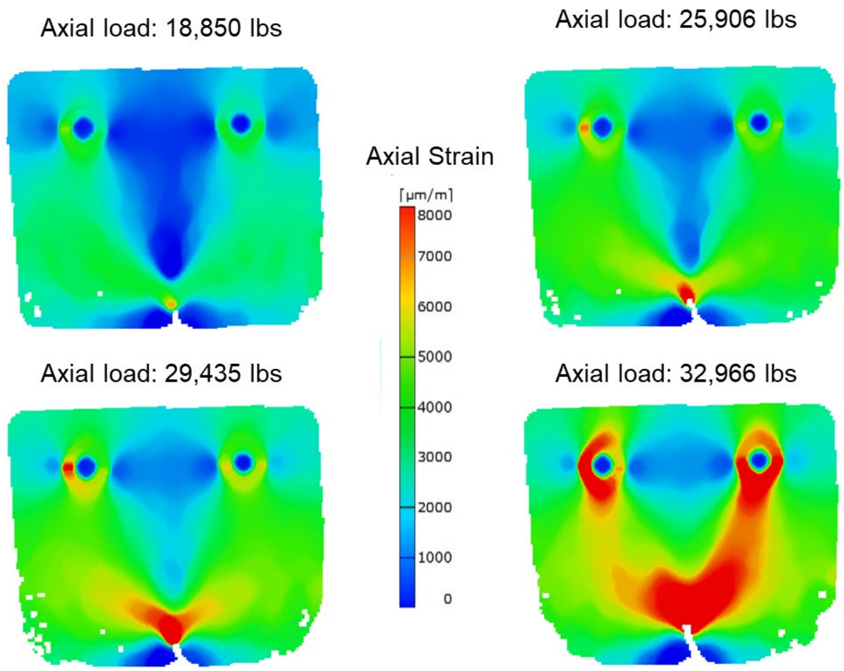

Figure 18. ARAMIS result during the circumferential direction limit load test

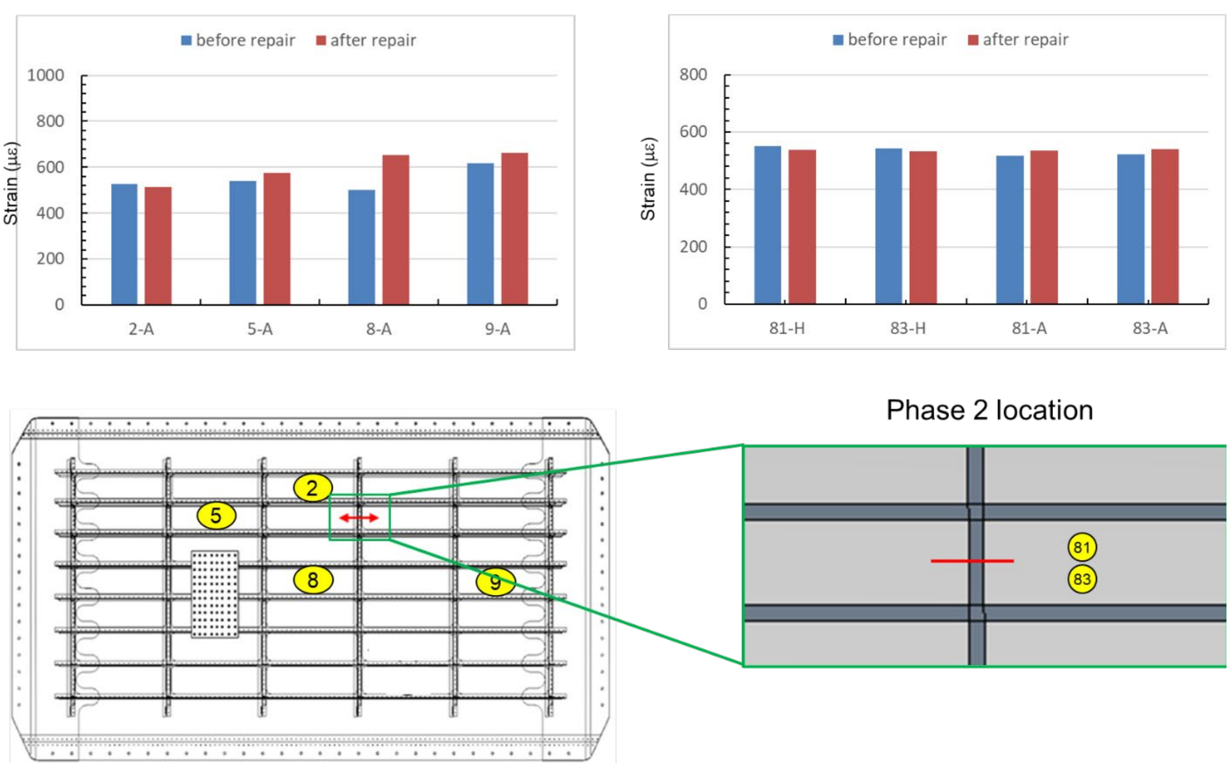

Figure 19. Strain survey after Phase 1 crack repair

4.2 Phase 2: Two-bay longitudinal notch with central frame severed

The longitudinal damage scenario for Phase 2 is shown in Figure 20. The frame F4 rivet at the mid-frame location between stringers S6 and S7 was removed, and frame F4 was severed at this location. Damage was simulated by cutting a 3.25-in. long notch in the skin above the severed F4 frame.

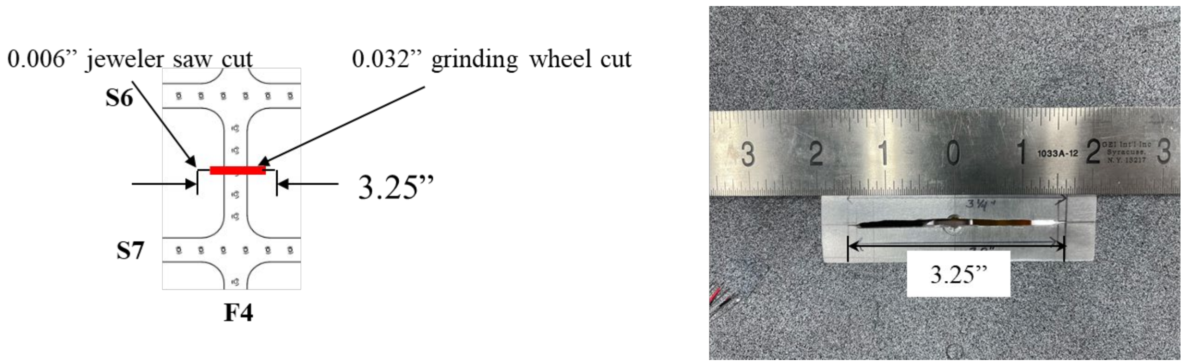

Figure 20. Configuration of Phase 2 damage scenario

For this phase, the panel was fatigue tested under pressure load conditions for 42,000 cycles, during which the skin crack extended across two frame bays to a final total length of approximately 12.5 in. The crack growth was slow in the initial stages of fatigue testing, and one side (right) was significantly slower than the other side (left) due to the crack binding, as shown in Figure 21. Consequently, the notch on the right side was extended using cutting wire to remove the binding portion of the crack front at around 9,000 cycles. After the removal of the crack binding, the fatigue crack growth was stable and continuous. The fatigue crack growth comparison among panels 1, 2, and 3 is shown in Figure 23. For an apples-to-apples comparison between the panels without the crack binding effect, the crack growth data for all three panels were shifted to the same crack length 2a = 3.85 in., as shown in Figure 24. Panel 3 still demonstrates similar damage tolerance performance to panel 2, and better than the baseline panel 1.

However, the right-side crack growth is still slower than the other side. Post-residual strength test investigation revealed that the asymmetrical crack growth was due to the transition of crack surface morphology resulting in crack growth-rate changes as observed during Phase 1 fatigue test, as shown in Figure 12. The left-side crack had slanted crack surface throughout the whole fatigue testing. However, the right-side crack transition from slant to V or less slant crack surface during the fatigue from approximately 18,000 to 28,000 shifted cycles (27,000 to 37,000 total cycles), as shown in Figure 22, which led to the slower crack grow. However, panel 3 exhibited better average crack growth performance compared to panel 1, as shown in Figure 23 and Figure 24.

During Phase 2 fatigue testing, two additional test segments were added, introducing cracks along the mill line. These test segments were designed to evaluate SHM systems' capability and reliability in a mill line crack scenario (Appendix E). The details of these SHM tests will be reported in a separate report. Furthermore, the frame end of F3 was unexpectedly broken at 32,900 cycles. The test panel was removed from the FASTER fixture and repaired (Appendix F). The panel was installed back on the FASTER fixture after the repair, and strain survey was conducted to ensure the frame repair did not change the load distribution in Phase 2 test area, as shown in Figure 25.

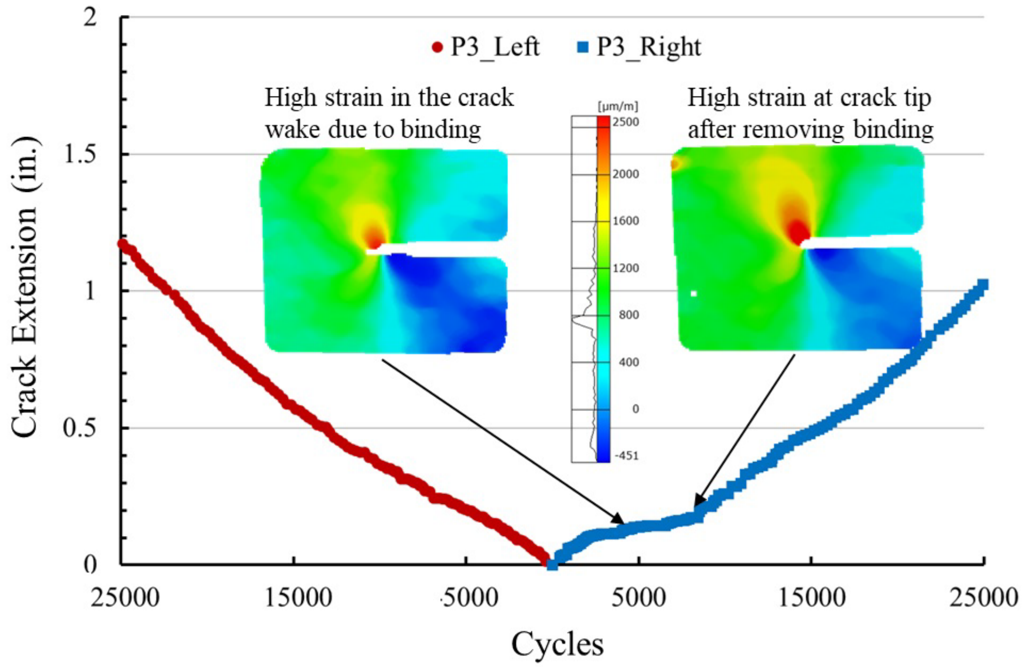

Figure 21. Slow fatigue crack growth on right side due to binding

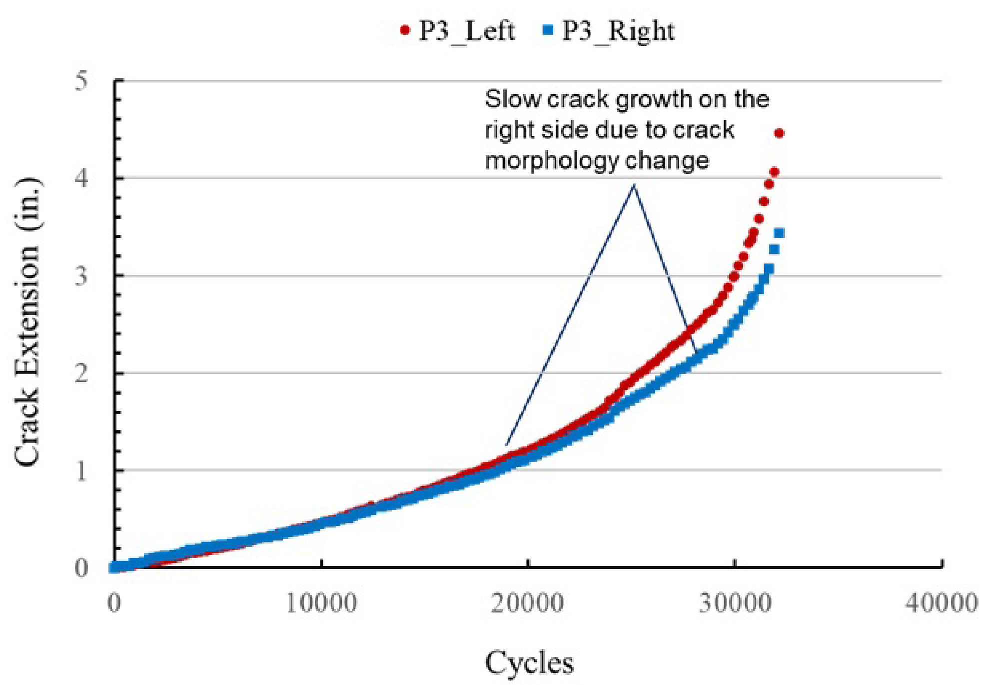

Figure 22. Slow fatigue crack growth on right side due to crack morphology change

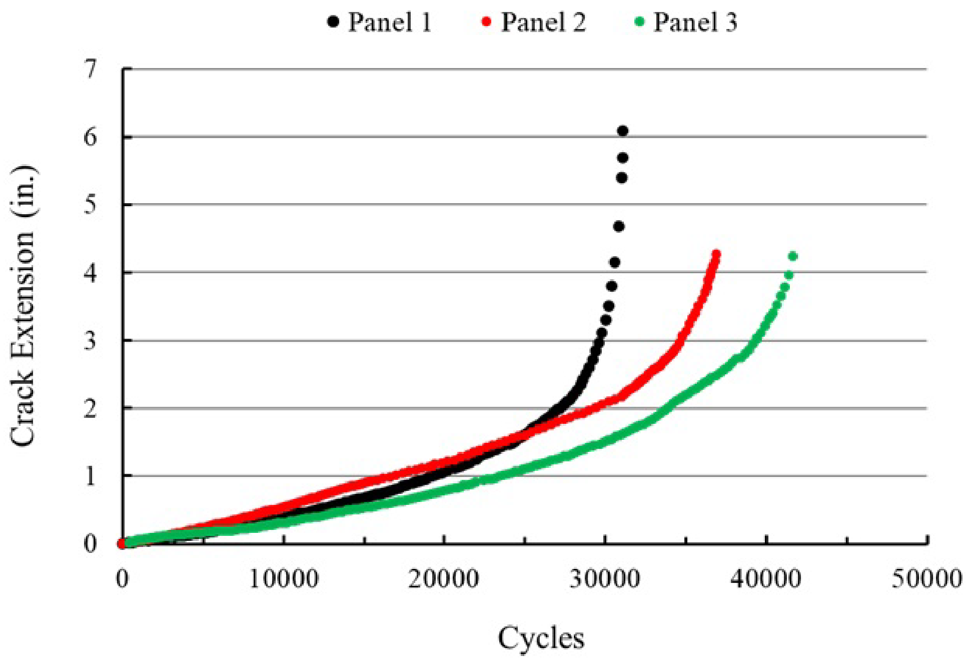

Figure 23. Average longitudinal crack growth comparison between panel 1, 2, and 3

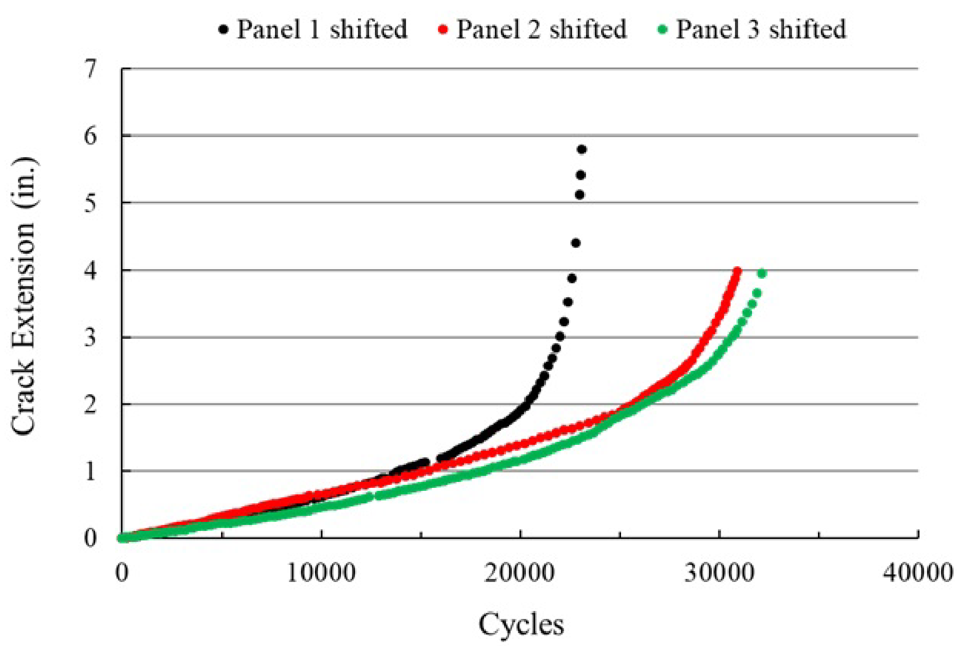

Figure 24. Average longitudinal crack growth comparison between panel 1, 2, and 3 after shifting data to remove crack binding effect

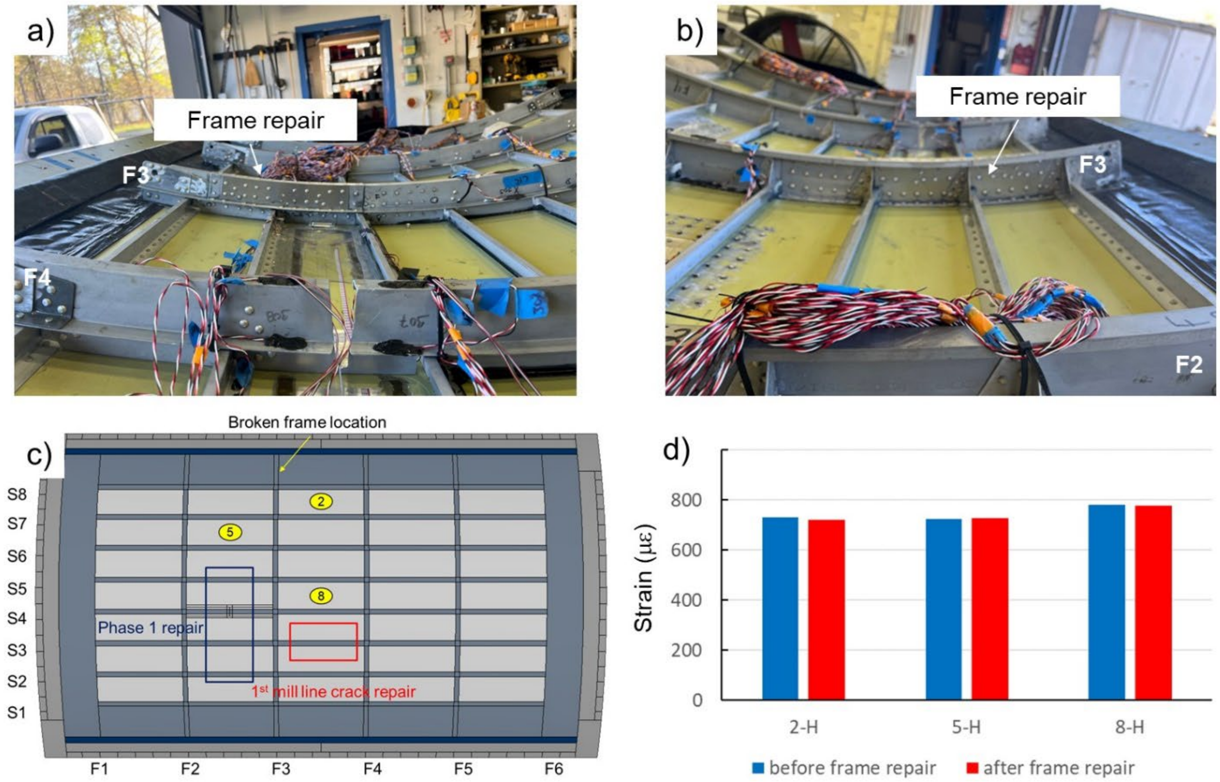

Figure 25. Frame repair and strain survey after frame repair

After fatigue testing, the final stage of testing was a residual strength test to certain limit load conditions identified in 14 CFR §25.571 (b) (Damage-tolerance... , 2023). The residual strength test was conducted under pressure loading applied quasi-statically. For panel 3, the team decided to conduct the residual strength test for a two full bay 40 in. crack condition. The fatigue test stopped at a crack length of about 12.5 in., the crack was extended with a saw cut all the way to the edge of the frame flange. The skin on top of the frame was then scribed as deeply as possible without damaging the frame attachment flange beneath it. The final damage configuration before the residual strength test is shown in Figure 26. Post-test photo and video analysis showed unstable tearing occurred at a maximum applied pressure of 13.3 psi, resulting in failure of the panel. The pre-test residual strength analysis demonstrates a good prediction of the failure pressure (Appendix G), as shown in Figure 27. Extensive damage occurred to the panel where the skin crack extended to a total length of 60 in., as shown in Figure 28. The pressure at failure exceeded the residual strength damage-tolerance requirements in 14 CFR §25.571 (b) (Damage-tolerance... , 2023).

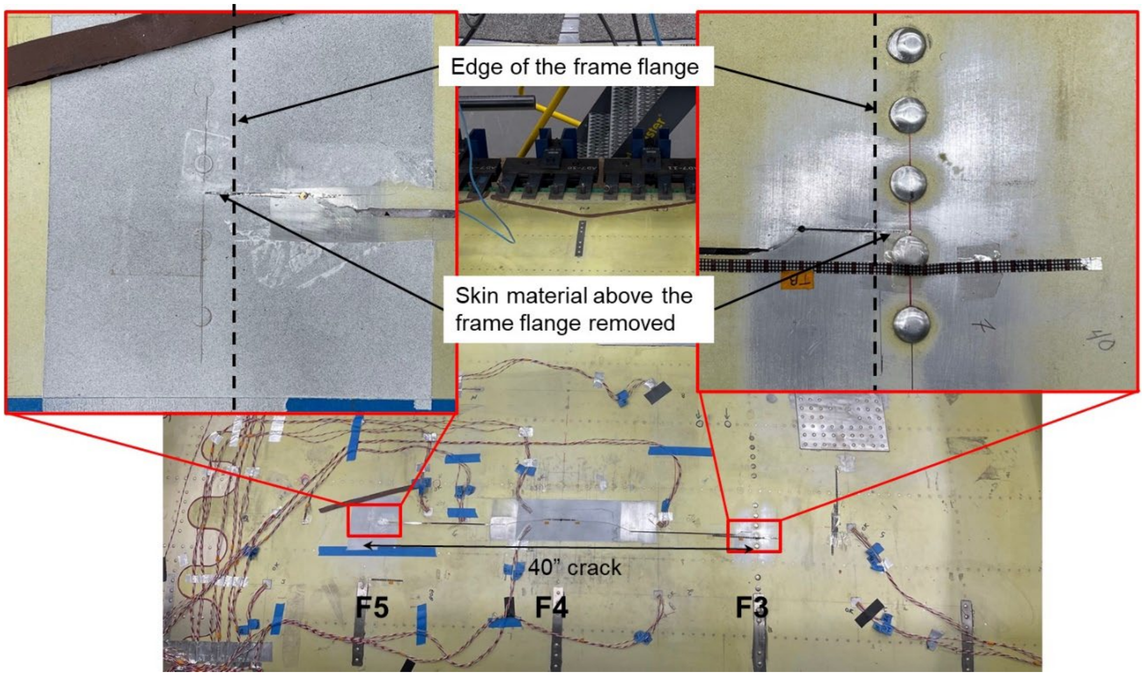

Figure 26. Final damage configuration before the residual strength test

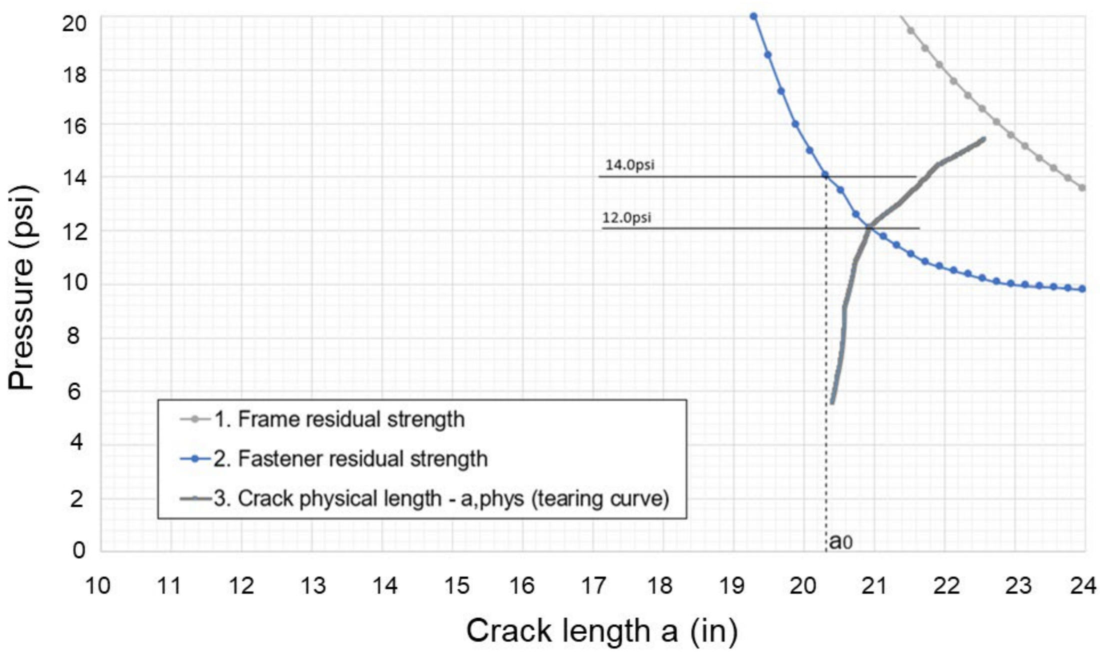

Figure 27. Analysis failure prediction

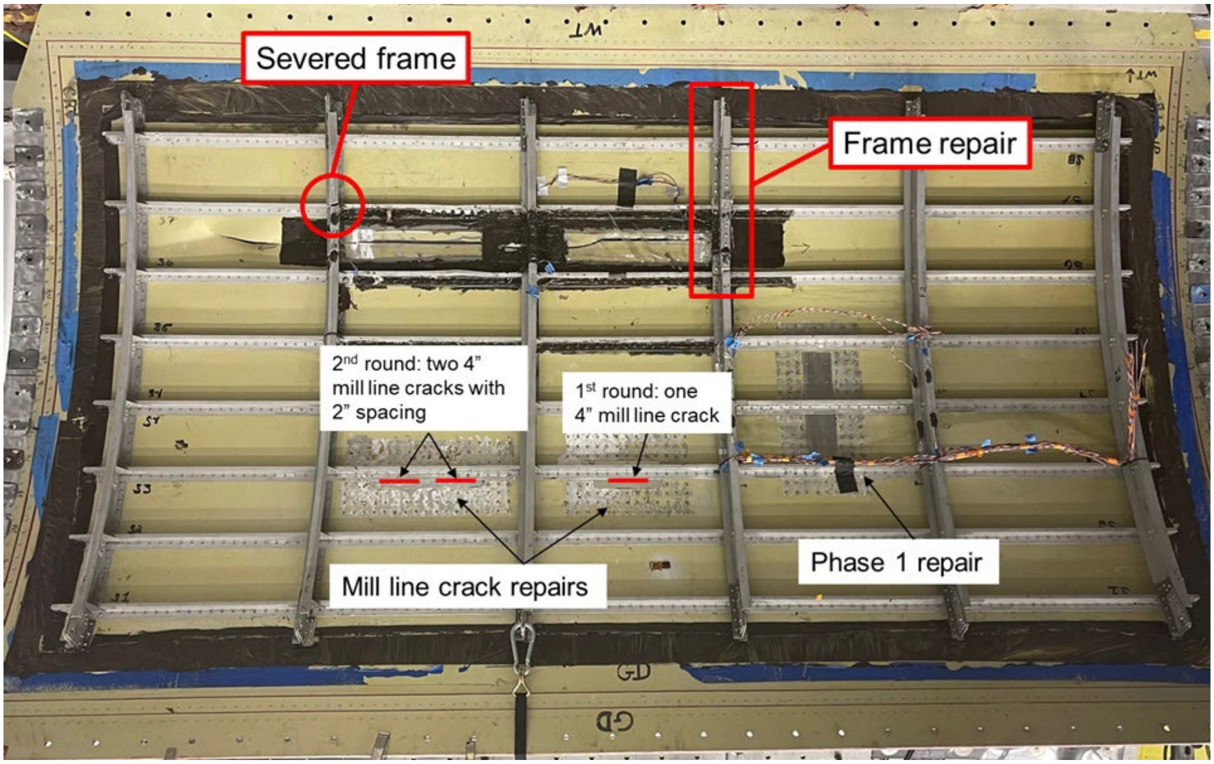

Figure 28. Picture of panel 3 after residual strength test

5 Summary

In a collaborative effort, the FAA, Arconic, and Embraer are assessing EMST for fuselage applications through full-scale test and analysis. Several technologies are being considered, including advanced Al-Li alloys and selective reinforcement using FMLs. Data from this study will be used to verify potential improved damage-tolerance performance and structural safety potential that EMST offer compared to the current fuselage structure constructed with conventional materials and fabrication processes, with a goal to provide guidance when considering EMST. This report documented results from panel 3 tests subjected to two phases of testing and accumulated 88,900 simulated flights.

Results from the panel 3 test compared to with the panel 1 and panel 2 and future tests on advanced panels containing varying EMST. Results and other major findings include:

- **Phase 1**: A two-bay circumferential crack-like notch having a total length of 1.3 in. was machined in the skin with the central stringer severed. The panel was then subjected to 46,900 fatigue cycles, during which slow and stable crack growth occurred to a final length of 11.3 in. Afterwards, a limit load test was conducted. Limited stable tearing extension was observed from each crack tip. Panel 3 exhibited similar damage tolerance behavior to panel 2 and showed approximately a 40% improvement in crack growth life compared to the baseline panel 1 in the circumferential damage scenario.

- **Phase 2**: A two-bay longitudinal crack-like notch was machined in the skin having a total length of 3.25 in. with the central frame severed. After 42,000 cycles of fatigue testing, the skin crack extended approximately to a total length of 12 in. Compared to the baseline panel 1, panel 3 exhibited approximately 45% improvement in crack growth life for this damage scenario. During the subsequent residual strength test, the panel failed at a pressure of 14 psi. This pressure exceeded the residual strength damage-tolerance requirements defined in 14 CFR §25.571 (b) (Damage-tolerance... , 2023).

6 References

Bertoni, M., Fernandez, F., & Miyazaki, M. (2014). Fuselage technology demonstrator. *Proceedings of AeroMat 2014.* Orlando, FL.

Beumler, T. (2014). Development of thin-walled FML-structures. *Proceedings of AeroMat 2014.* Orlando, FL.

Chaves, C. (2017). A review of aeronautical fatigue investigations in Brazil. *Proceedings of the 35th ICAF Conference.* Nagoya, Japan.

Damage-tolerance and fatigue evaluation of structure, 14 CFR § 25.571 (2023). Retrieved from https://www.govregs.com/regulations/14/25.571

Eberl, F., Smith, P., Layel, J., Fernandez, F., Nunes, D., Cruz, M., . . . Garcia, J. (2015). Manufacturing of a novel upper wing cover demonstrator using friction stir welding. *Proceedings of AeroMat 2015.* Long Beach, CA.

Flugge, W. (1952). *Stress problems in pressurized cabins.* NACA Technical Note.

Heinimann, M., Kulak, M., Bucci, R., James, M., Wilson, G., Brockenbrough, J., . . . Sklyut, H. (2007). Validations of advanced metallic hybrid concepts with improved damage tolerance capabilities for next generation lower wing and fuselage applications. *Proceedings of the 24th ICAF Symposium.* Naples, Italy.

Kok, L., Poston, K., & Moore, G. (2011). Bombardier aerospace FSW demonstrator. *Proceedings of the 26th ICAF Symposium.* Montreal, Canada.

Kulak, M., Bakuckas, J., Tian, Y., Stanley, D., Chang, P., Sklyut, H. (2022). *Design, analysis and test development of full-scale fuselage test panels to assess emerging metallic structures technologies [DOT/FAA/TC-24-40].* Federal Aviation Adminstration.

Lowak, H., de Jonge, J., Franz, T., & Schutz, D. (1979). *MINITWIST - A shortened version of TWIST.* NLR Report No. TB-146.

Prasad, N., Gokhale, A., & Wanhill, R. (. (2014). *Aluminum-lithium alloys, Processing, properties, and applications.* Elsevier.

Schmidt, H. (2005). Damage tolerance technology for current and future aircraft structure. *Proceedings of the 23rd ICAF Symposium.* Hamburg, Germany.

Silva, D., Cruz, M., Mendonca, W., Brandao, F., Sakata, A., Silva, G., & Kulak, M. (2017). Manufacturing of a fiber metal laminate lower wing cover demonstrator. *Proceedings of AeroMat, 2017.* Charleston, SC.

Steadman, D. (2007). *Destructive evaluation and extended fatigue testing of retired transport aircraft [DOT/FAA/AR-07/22 V5].* Volume 5: Data Analysis Report. Federal Aviation Administration.

Stonaker, K., Bakucka, W. I., & Freisthler, M. (2015). Material characterization of aluminum lithium alloys used in aerospace applications. *Proceedings of the 28th ICAF Symposium.* Helsinki, Finland.

Stonaker, K., Bakuckas, J., Stanley, D., Kulak, M., Chang, P., & Freisthler, M. (2019). Assessment of fatigue behavior of advanced aluminum alloys under complex variable amplitude loading. *Proceedings of the 30th ICAF Symposium.* Krakow, Poland.

Tian, Y., & Backuckas, J. (2019). *Full-scale aircraft structural test evaluation and research (FASTER) fixture [DOT/FAA/TC-TN19/6].* Federal Aviation Administration.

Tian, Y., Stanley, D., & Backuckas, J. (2021). *Assessment of emerging metallic structures technologies through test and analysis of fuselage structure: Test panel 1[DOT/FAA/TC21-25].* Federal Aviation Administration.

Tian, Y., Stanley, D., & Backuckas, J. (2023). *Assessment of emerging metallic structures technologies through test and analysis of fuselage structure: Test panel 2[DOT/FAA/TC23-24].* Federal Aviation Administration.

A Panel 3 geometry

The skin, frame and stringer geometry described in this Appendix were selected from a crown location forward of the wing centerline. At this location, the panel geometry was equally critical for crack growth circumferentially and longitudinally, and the same geometry would be relevant for axial and longitudinal loading.

The materials in the baseline Panel 3 are described in Table 2. The geometry was determined using the sizing methods described by Kulak (2024) using the materials in Table 2.

The overall panel design is shown in Figure A-1. The panel length is approximately 125 in., and the length of the panel arc is 76.5 in. with a vertical projection of 73.2 in.

Engineering drawings used for Panel 3 construction are the same as Panel 2 except the skin material and thickness.

Fuselage Skin Sheets

The fuselage skin for the baseline panel 3 utilized a 2029-T3 sheet. The skin was supplied in a gage of 0.09 in. and was bare sheet. The final skin thickness in the stringer and frame attachment landings was 0.065 in., and the skin was pocketed to 0.053 in. (see Figure A-2). The rivets on the airflow side of the fuselage panels for the skins, stiffeners, and frames were the 100-degree countersunk fastener NAS1097AD-5, which has a 5/32-in. diameter (AD = 2117-T4 rivet). For the stringer clips in panel 3, the universal head rivet MS20470AD-5 (5/32-in. diameter, 2117-T4) was used.

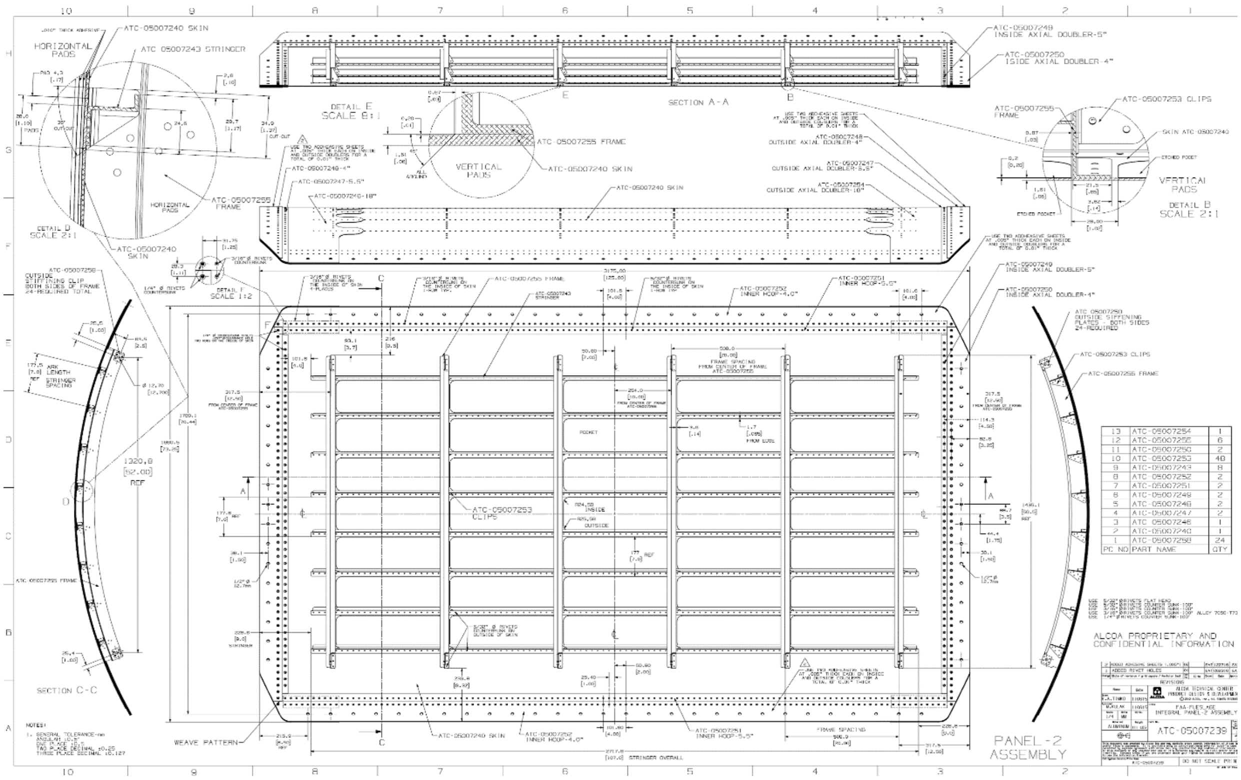

Figure A-1. Panel 3 overall dimensions

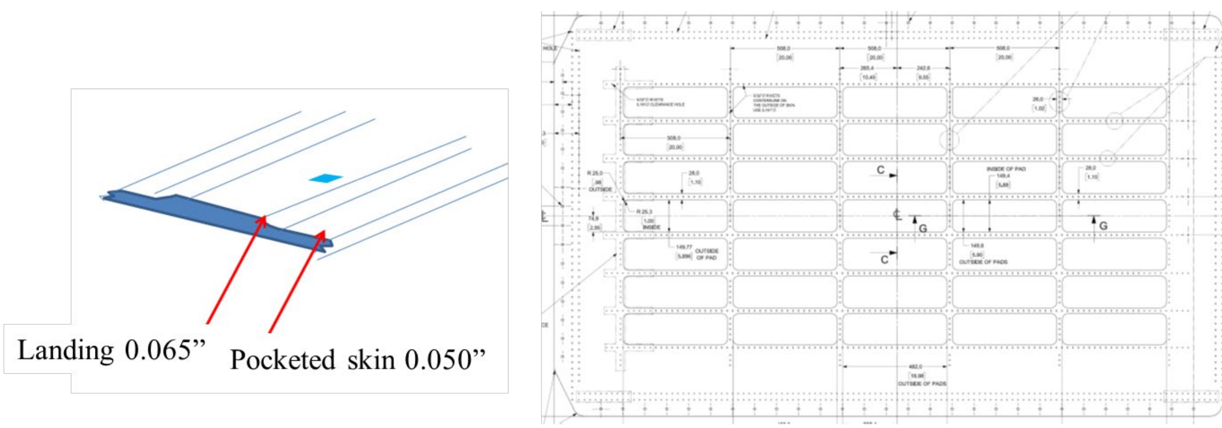

Figure A-2. Pocketed skin

Panel 3 Load Introduction Doublers and Bonding to Skins

For panel doublers, a higher-strength 7xxx sheet, like 7075-T6, was used (non-clad). The edge doublers package on both the inside and outside of the fuselage panel were roll formed to curvature. The doubler package was prepared for bonding to the skins.

The doublers were bonded to the skin, using either an oven-cured epoxy like FM73 or a cold bonding adhesive. In addition, countersunk Huck bolt or Lock bolt fasteners were used to secure all edge doublers.

After chemical milling, the panel underwent the appropriate surface treatment procedure—in stringer frame landings and pocketed regions—to protect the panel against corrosion and allow sealant to be used under the frame and stringer areas, which are riveted to the skin. After chemical milling, the pocketed regions were anodized and primed.

Stringer clip

The frame system for Panel 3 utilized a one-piece integral frame construction, where the integral frame is attached to the skin directly and to stringer via a stringer clip, as shown in Figure A-3. The stringer clip used 7075-T62.

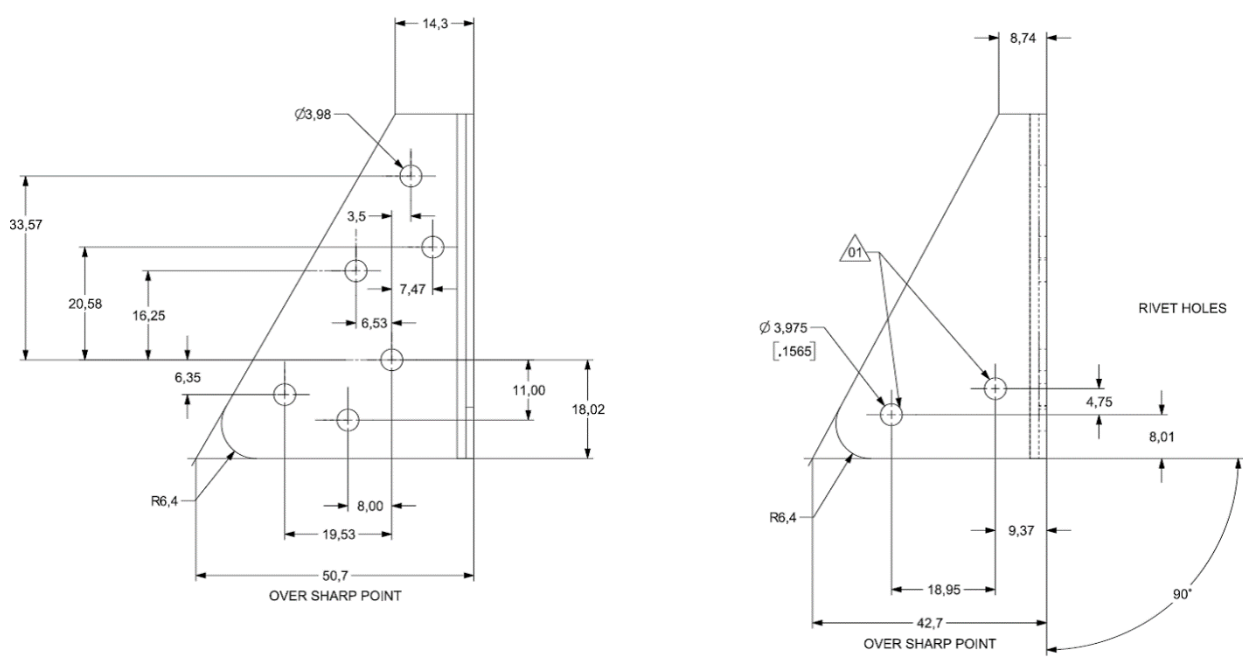

Figure A-3. Stringer clip

Frame

The frame, as shown in Figure A-4 was riveted directly to the skin and stringer through stringer clips using the previously identified fasteners. The frame was made of 2099-T83 extrusions alloy. The frame was stretch formed to a constant radius reflecting the offset from the skin radius.

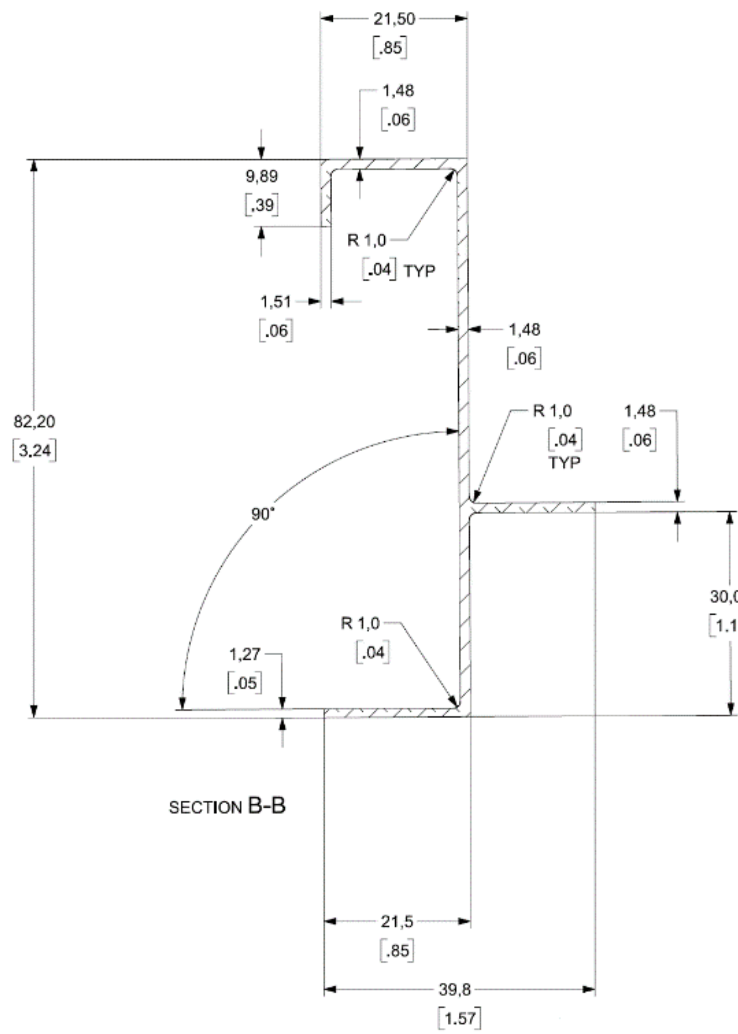

Figure A-4. Frame

Stringer

The stringers were made of 2055-T84 extrusions. The Z cross-section was extruded with attach flanges of a radius to match the 74-inch-radius curve of the panel, as shown in Figure A-5.

Loading and doublers

The test panel was loaded through the skin by actuators axially and in the hoop direction. The frames were also loaded in the hoop direction at each frame end by individual actuators. The test panel was loaded internally by pressure. See panel 2 report for details of assembly drawing and doublers at panel edges and frame end load attachment points (Tian, Stanley, & Backuckas, DOT/FAA/TC-TN/23/24, 2023).

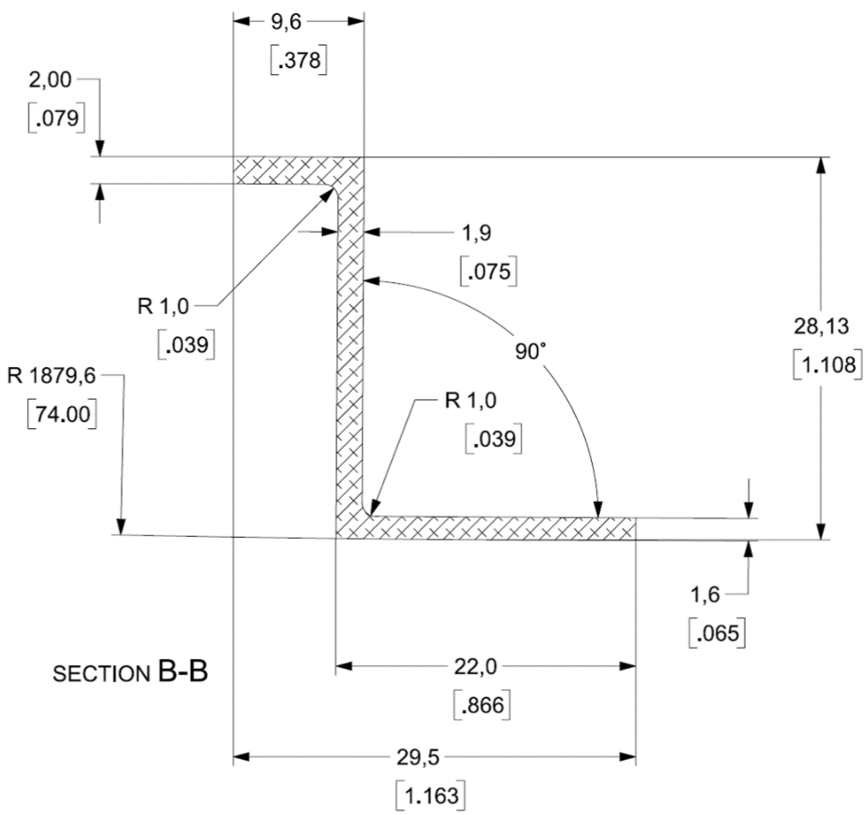

Figure A-5. Stringer

B Phase 1 repair

At the end of Phase 1, the cracked structure needed to be repaired in order to continue with the testing phase. Phase 1 crack was repaired using Boeing 727 structural repair manual 53–30–3 as a guideline. This appendix provides some details of the procedure and material used for the installation of SRM repairs.

Figure B-1 shows the location of the SRM repair on Panel 3. Before the installation of the SRM repair, the surface of the skin was cleaned with acetone and dry air to remove any contaminants. Next, the eddy current system was used to mark the crack tips for both crack locations.

After marking the crack tips, further procedures were followed in accordance with the B727 SRM skin repair instructions. The basic requirement is that for a minimum of three rows of rivets beyond the damage cutout, the repair doubler should be one gage thicker than the skin material and it is acceptable to use button head rivets instead of countersunk rivets, as shown in Figure B-2. Figure B-3 shows the actual image of the SRM repairs after installation from both sides.

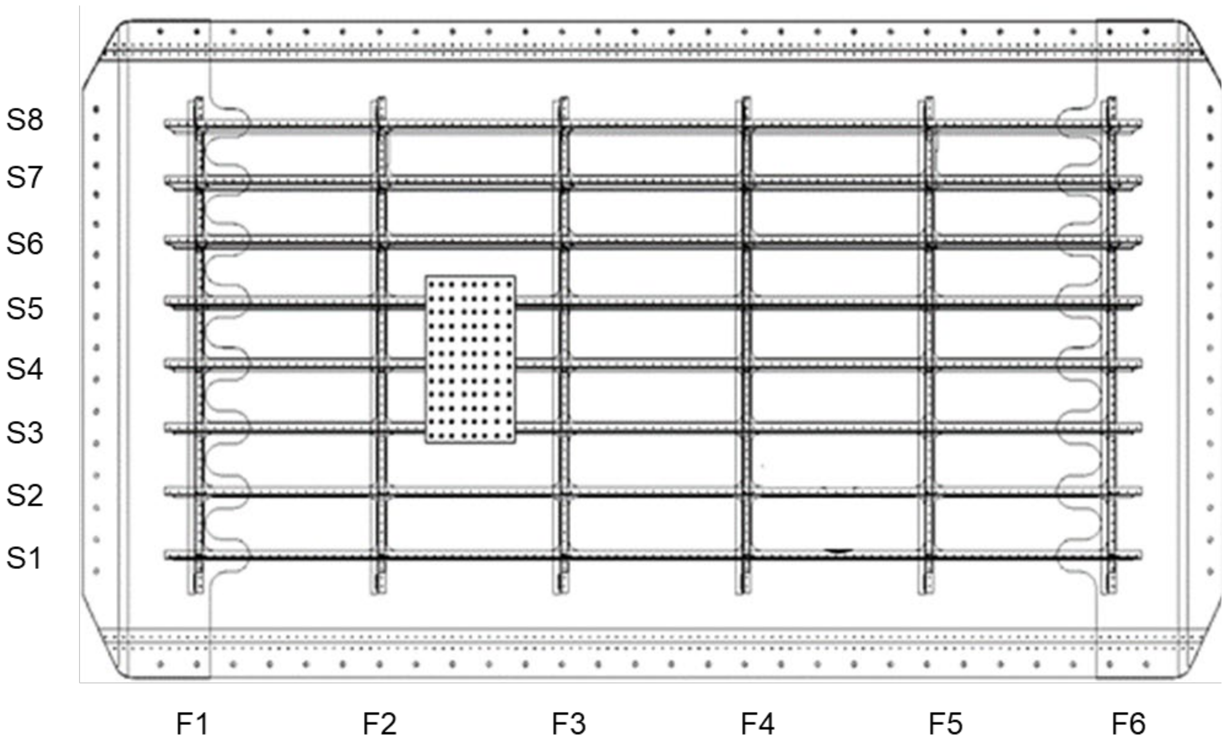

Figure B-1. Location of Phase 1 SRM repair

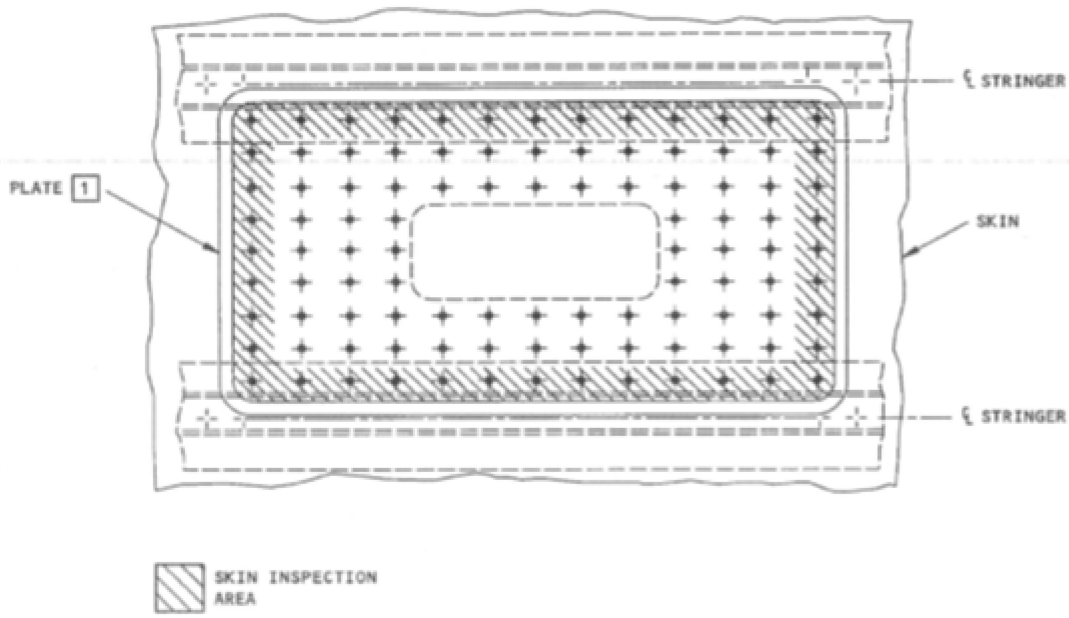

Figure B-2. Typical SRM skin repair configuration

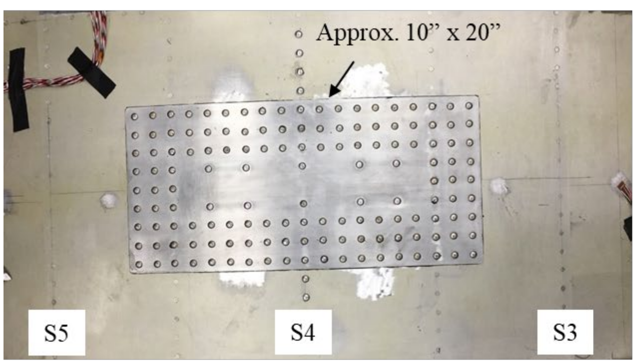

External view

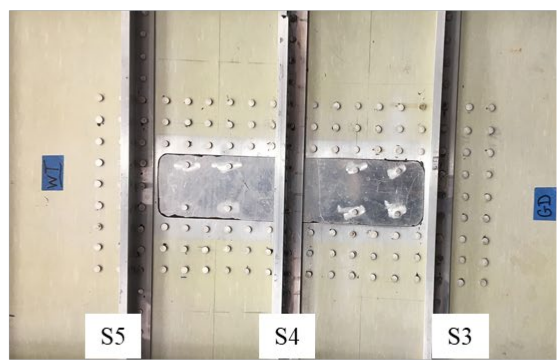

Internal view

Figure B-3. Phase 1 repair external and internal views

C Strain gage instrumentation

The test panel was fully instrumented with strain gages within the test section to provide for real-time monitoring of the panel strain distributions, as shown from Figure C-1 to Figure C-4. The locations of strain gages installed on the skin, frames, and stringers for each test phase are provided from Figure C-5 to Figure C-10.

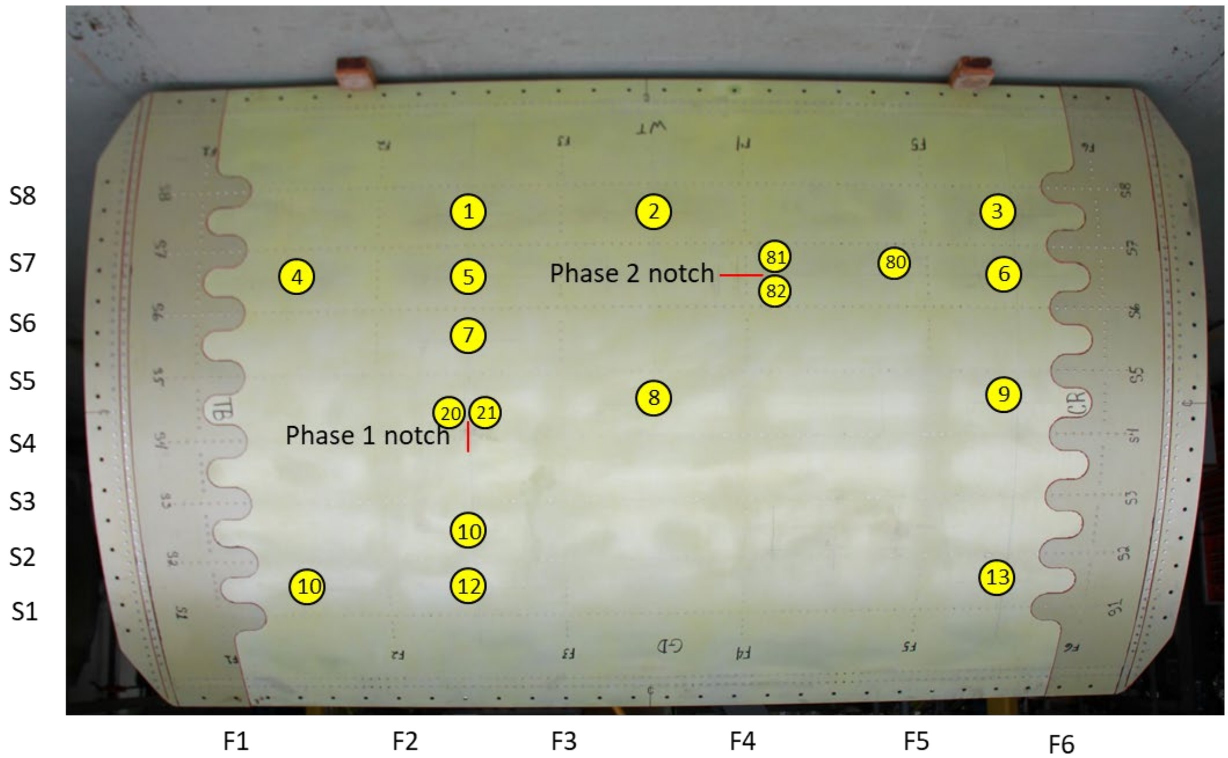

Figure C-1. Picture of external rosette gages

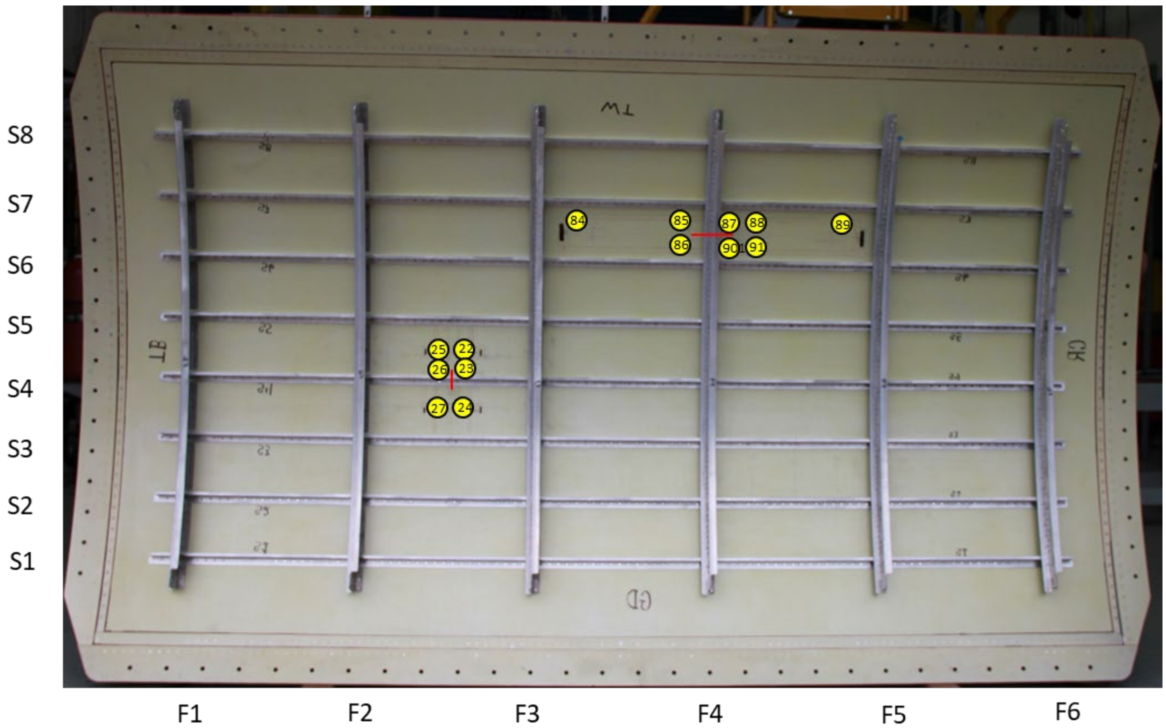

Figure C-2. Picture of internal rosette gages

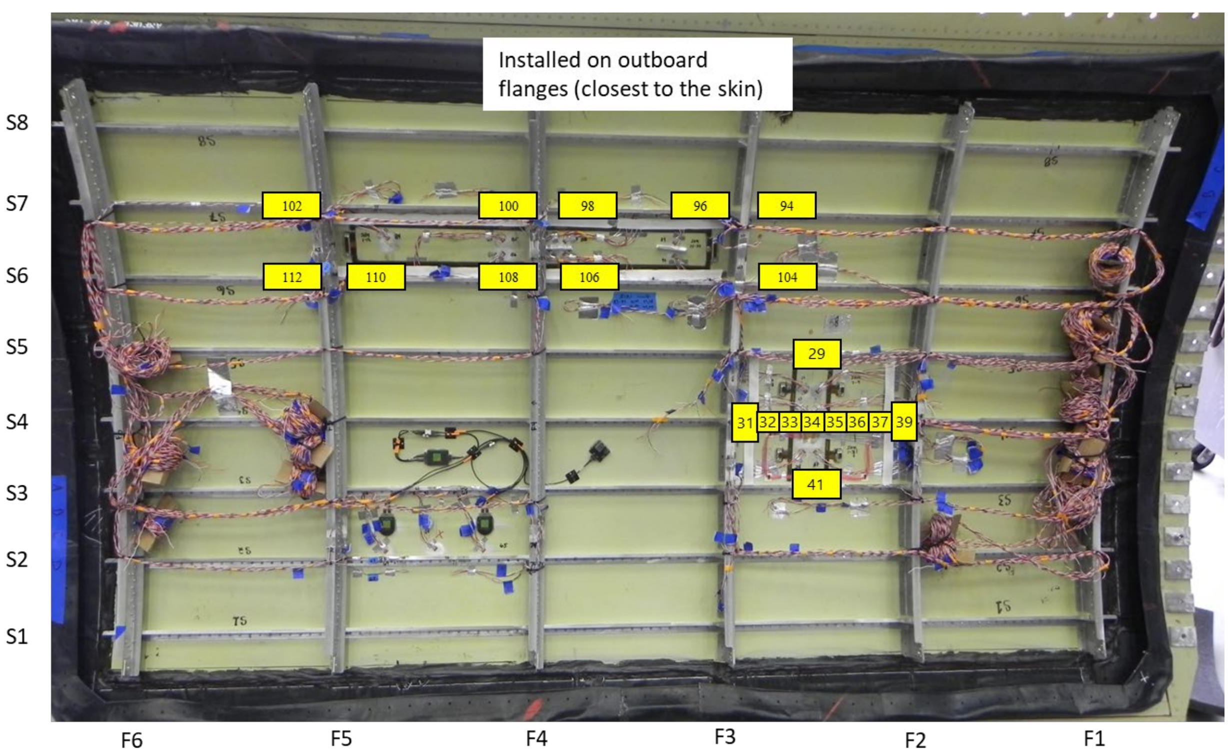

Figure C-3. Picture of stringer gages

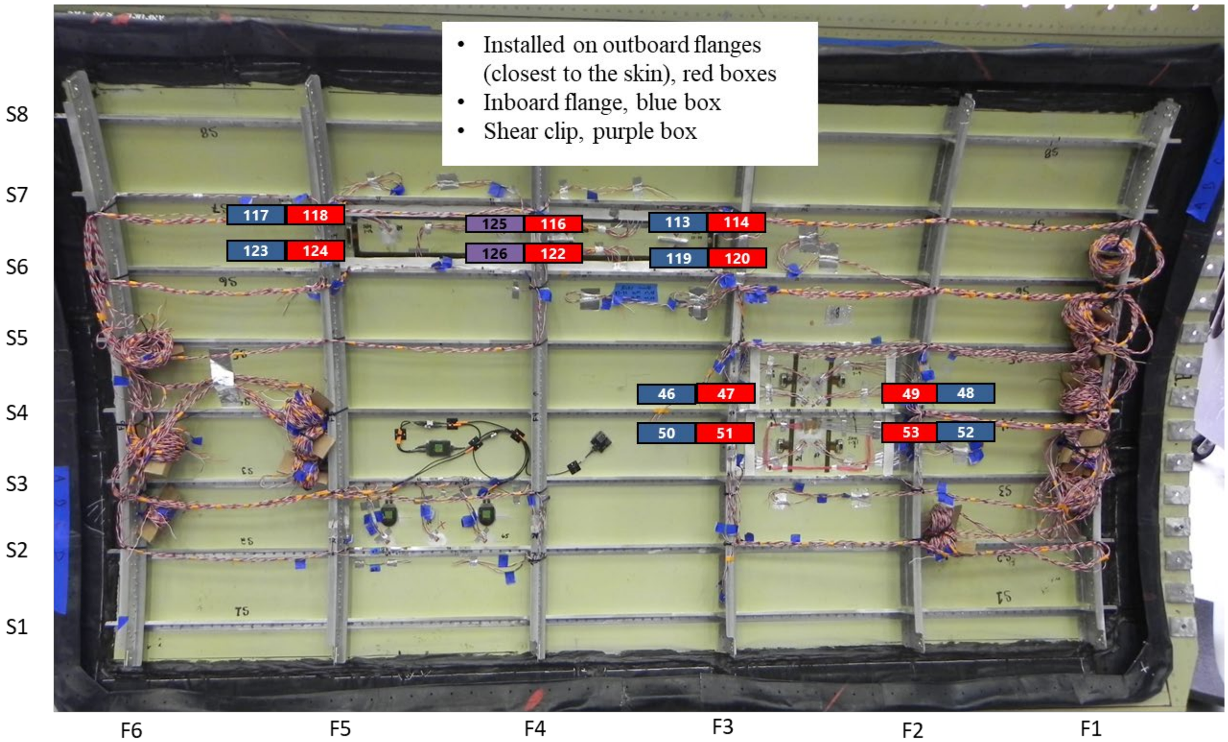

Figure C-4. Picture of frame gages and stringer clip gages

Strain readings were recorded during holds occurring at equal load intervals up to the maximum applied loads during strain surveys. In addition, data was continuously recorded at a frequency of 1 Hz and at each endpoint to monitor the strains during the test. Strain gages at mid-bay locations that were monitored throughout all phases are shown in Figure C-5.

The test panel was instrumented with strain gages to meet the following considerations:

1. Strain gages were strategically placed on the test panel to compare with the FEM analysis results. The gages were placed on the skins, stringers, and frames for the circumferential crack and longitudinal crack, to confirm the variation in stress in these critical areas before cracks are inserted.

2. The gages were placed strategically close to the crack tip to confirm stresses once cracks start growing.

3. Strain gages were also placed at other strategic locations of the panel to compare with the FEM results based on prior experience the FAA has gained from testing panels.

The wires for strain gages that pass through the inside of the pressure box were Teflon-coated to prevent water damage. A lead wire minimum length of 15 feet extending outside the pressure box was soldered to each strain gage channel. Readouts for all strain gages were monitored periodically and permanently recorded during the fatigue test and during strain survey under mechanical loading.

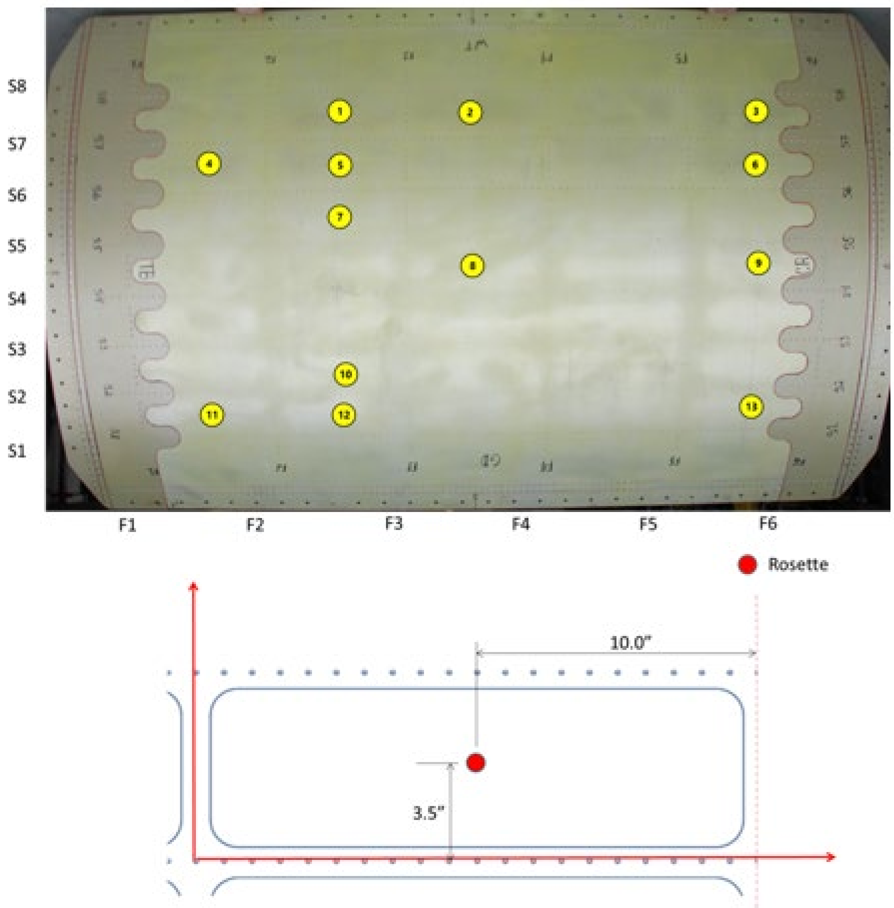

Figure C-5. Mid-bay location strain gages

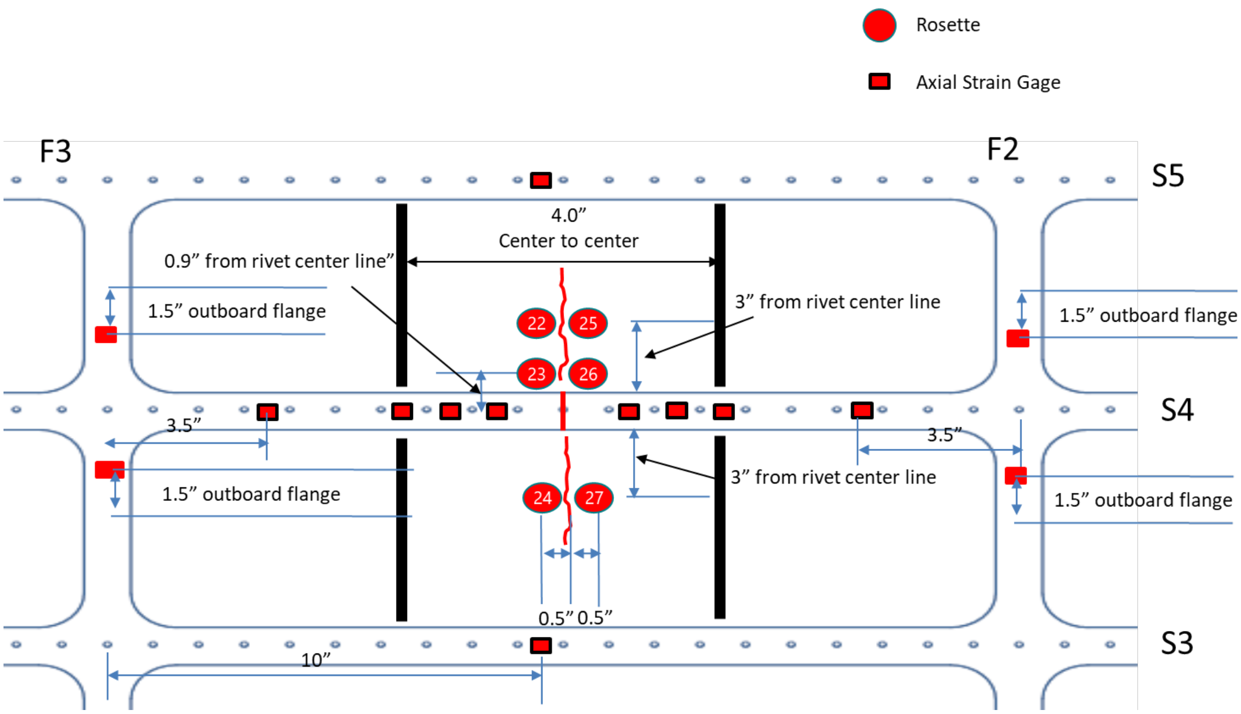

Figure C-6. Phase 1 internal gages

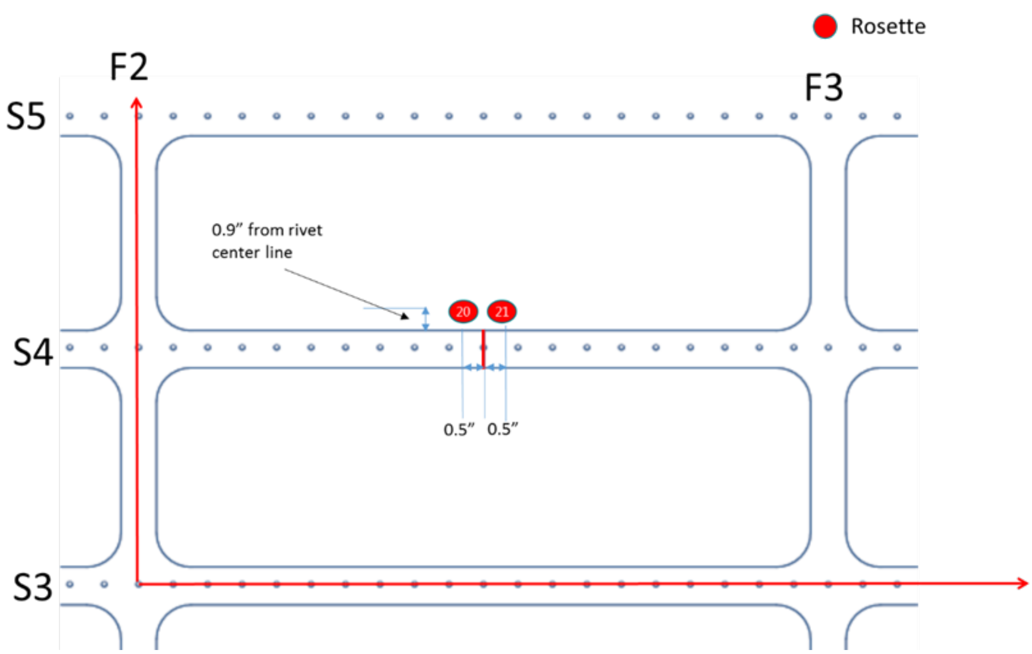

Figure C-7. Phase 1 external skin gages

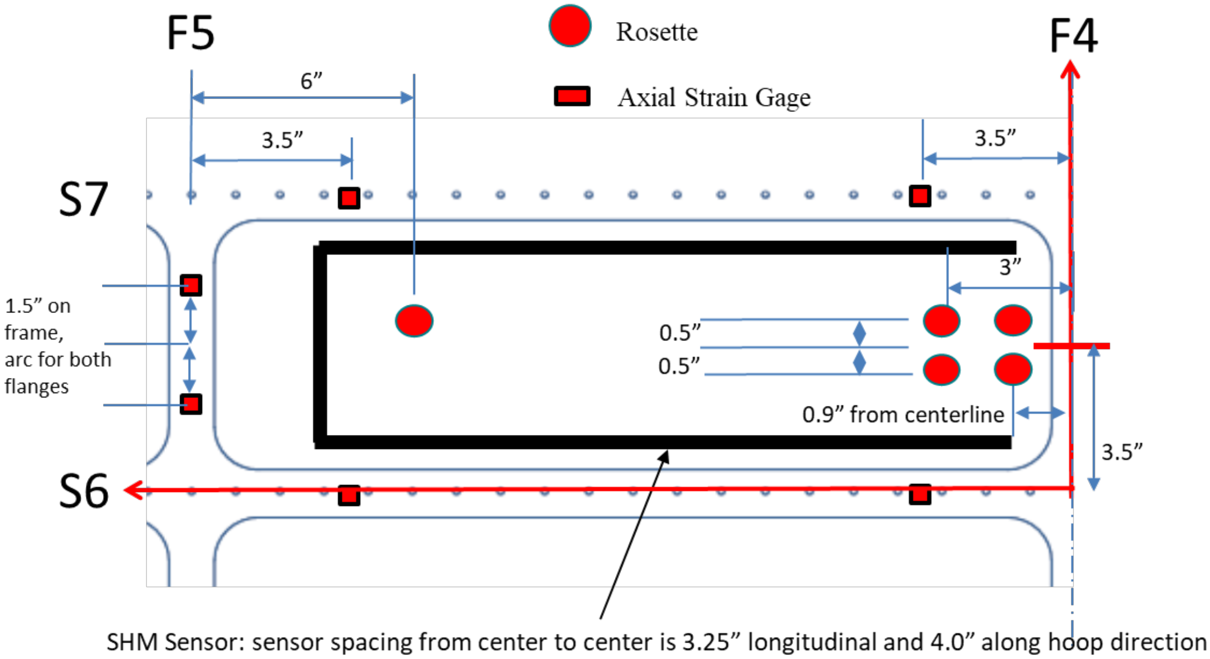

Figure C-8. Phase 2 internal gage: left side

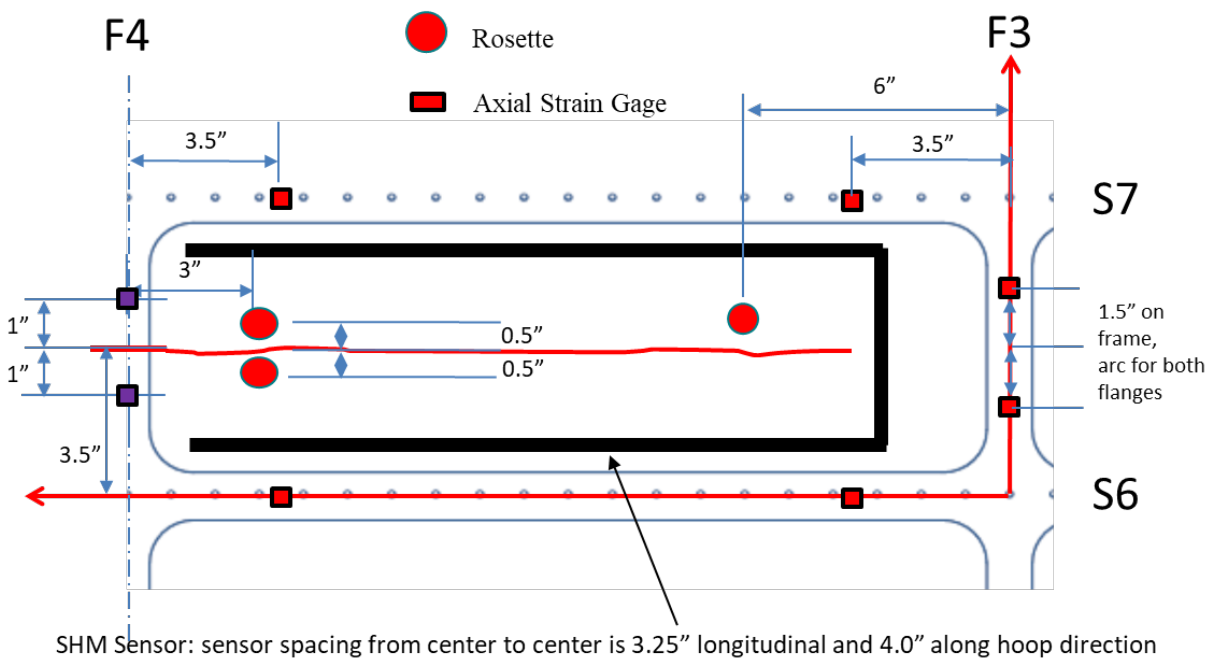

Figure C-9. Phase 2 internal gages: right side

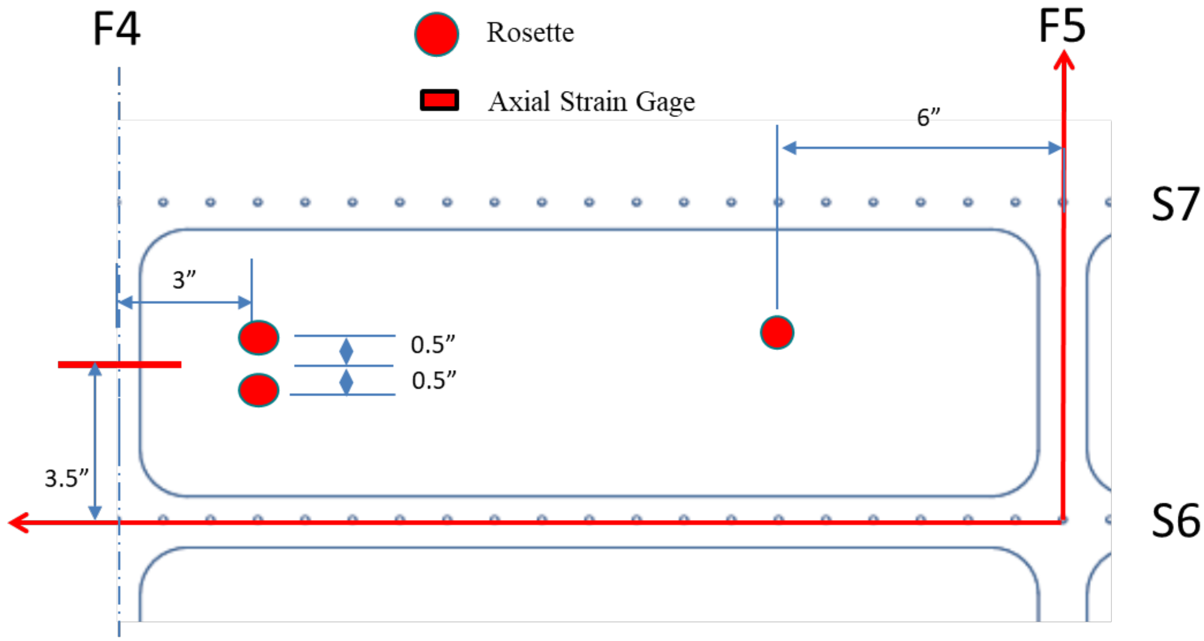

Figure C-10. Phase 2 external gages

D ARAMIS digital image correlation system

Full-field deformation and strain data were recorded during the loading of the test panels using the ARAMIS™ three-dimensional digital image correlation (DIC) system. The system, which uses two 5-megapixel cameras, is capable of accurately measuring full-field strain. The typical system setup and stochastic pattern used are shown in Figure D-1.

Prior to testing, the areas to be monitored by the photogrammetry system were coated with a high-contrast, stochastic speckle pattern. Flat-black spray paint was used to create a random pattern on top of a flat white layer. Baseline images were taken using both cameras at zero loads. Deformed images were recorded using both cameras while under an applied load. The baseline and deformed images are then used to determine the full-field deformation and strain field.

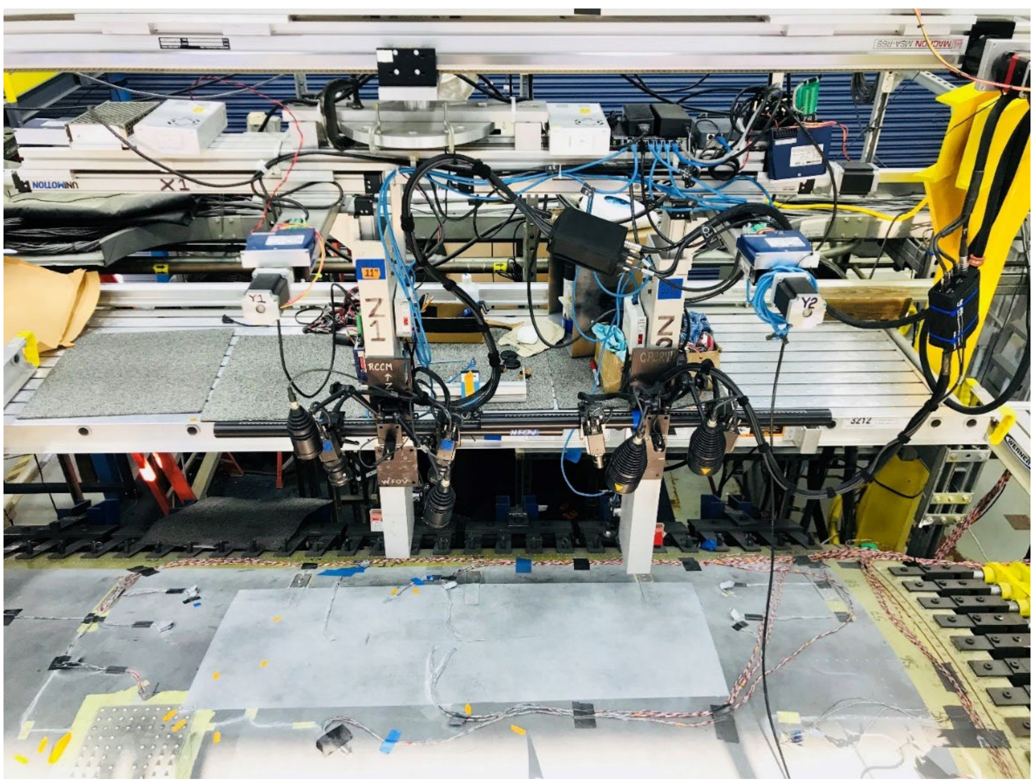

Figure D-1. ARAMIS system setup and stochastic pattern on panel

E Structural health monitoring system

Several structural health monitoring (SHM) systems were tested for different damage scenarios during Panel 3 fatigue testing: 1) an Acellent system and a Metis design system for Phase 1 circumferential cracks, and Phase 2 longitudinal cracks, 2) Acellent and Metis design systems for the first mill line crack case and 3) an Acellent and dFinder fiber optics systems for the second mill line crack case, as shown from Figure E- 1 to Figure E- 4.

The sensors were installed by FAA personnel following the OEM instructions, which is similar to bonding strain gage in terms of surface preparation and time required. Sensor locations and cable routing were designed to prevent interference with strain gages and were connected to corresponding data acquisition units. The SHM data was collected periodically during the inspection and strain surveys. The details of sensor description and installation procedure for Acellent and Metis systems were provided in .

Two rounds SHM study for the mill line crack scenario were added in the middle of Phase 2 fatigue testing. The FEM analysis was conducted to ensure the introduction of these mill line cracks will not affect the loads in the Phase 2 test area. A single mill line crack was introduced at 10,000 cycles for the first round. The initial crack length was 4 in. Acellent PTZ sensors were installed on one side of crack tip, and Metis carbon nanotube sensor was installed on the other crack tip, as shown in Figure E- 4. This phase of SHM testing was stopped when crack extended about 1 in. around 16,000 cycles, and damaged area was repaired. Two mill line cracks were introduced at 38,250 cycles for the second round, which consisted of two 4 in. long mill line cracks with 2 in. gaps between them. The Acellent sensors were installed on one side while fiber optics were installed on the other crack tip, as shown in Figure E- 4. The second round of mill line SHM study was stopped at 40,250 cycles, just before the conclusion of longitudinal crack fatigue testing. The details of this study will be published in a separate report.

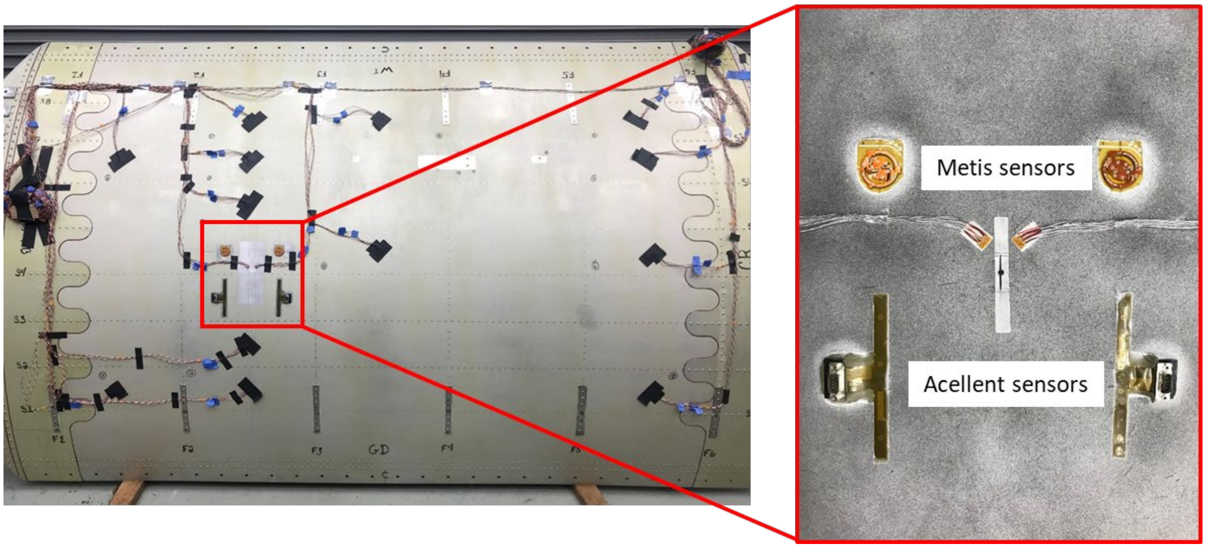

Figure E- 1. SHM sensor locations for panel 3 phase 1 circumferential crack

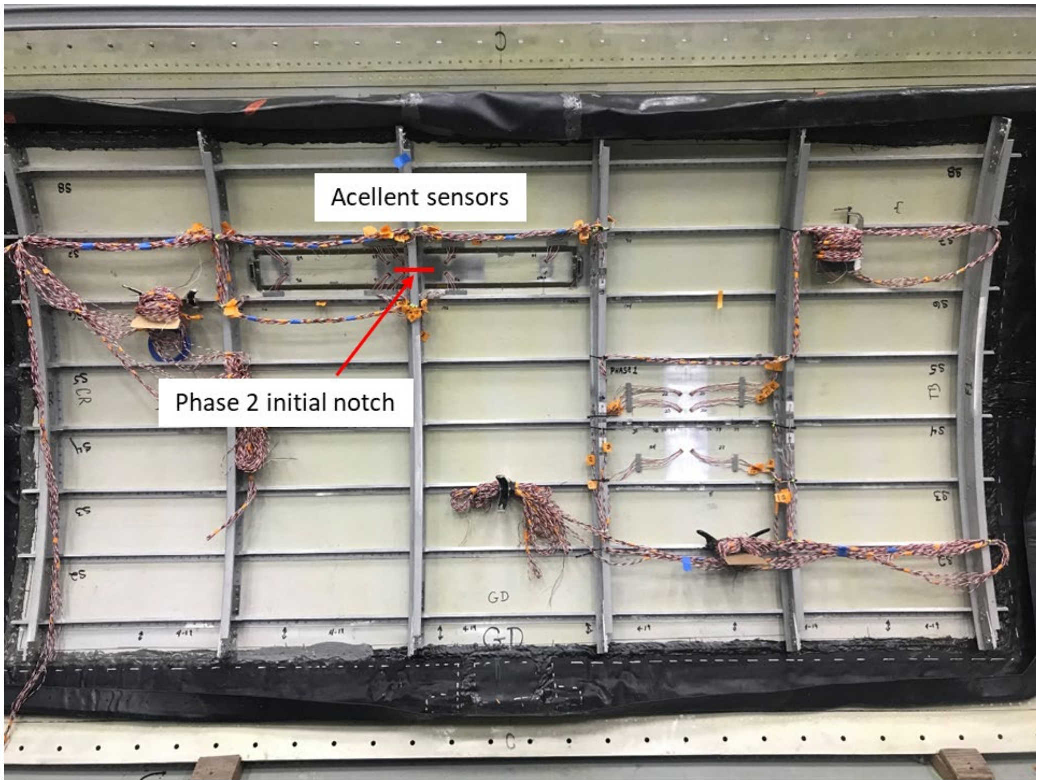

Figure E- 2. SHM sensor locations for panel 3 phase 2 longitudinal crack

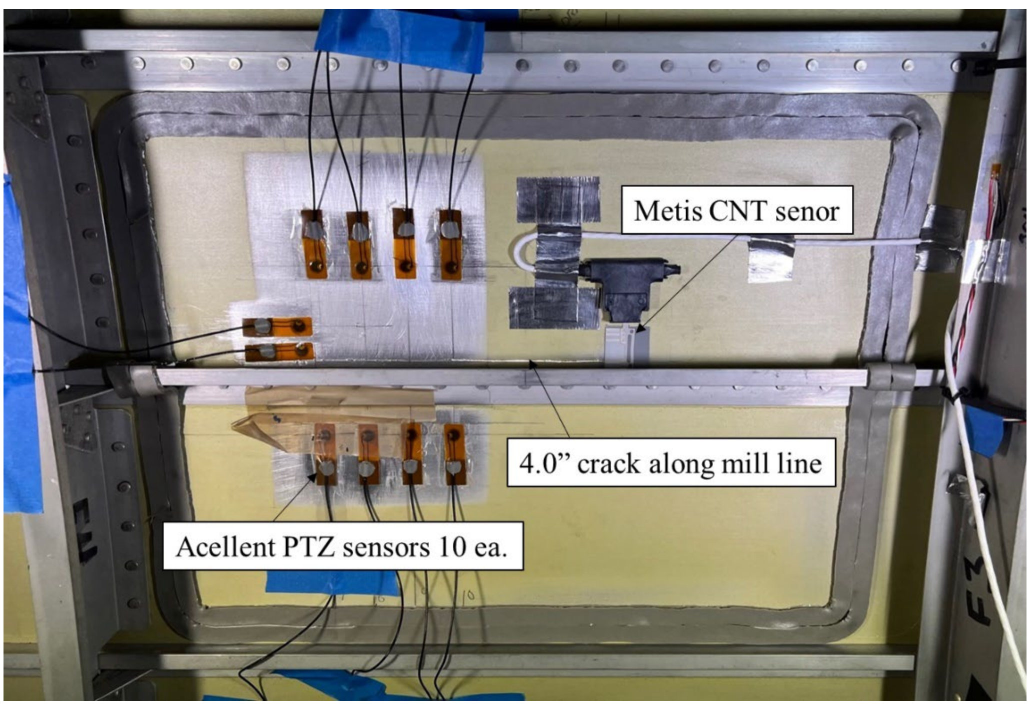

Figure E- 3. SHM sensor locations for the first-round mill line crack SHM study

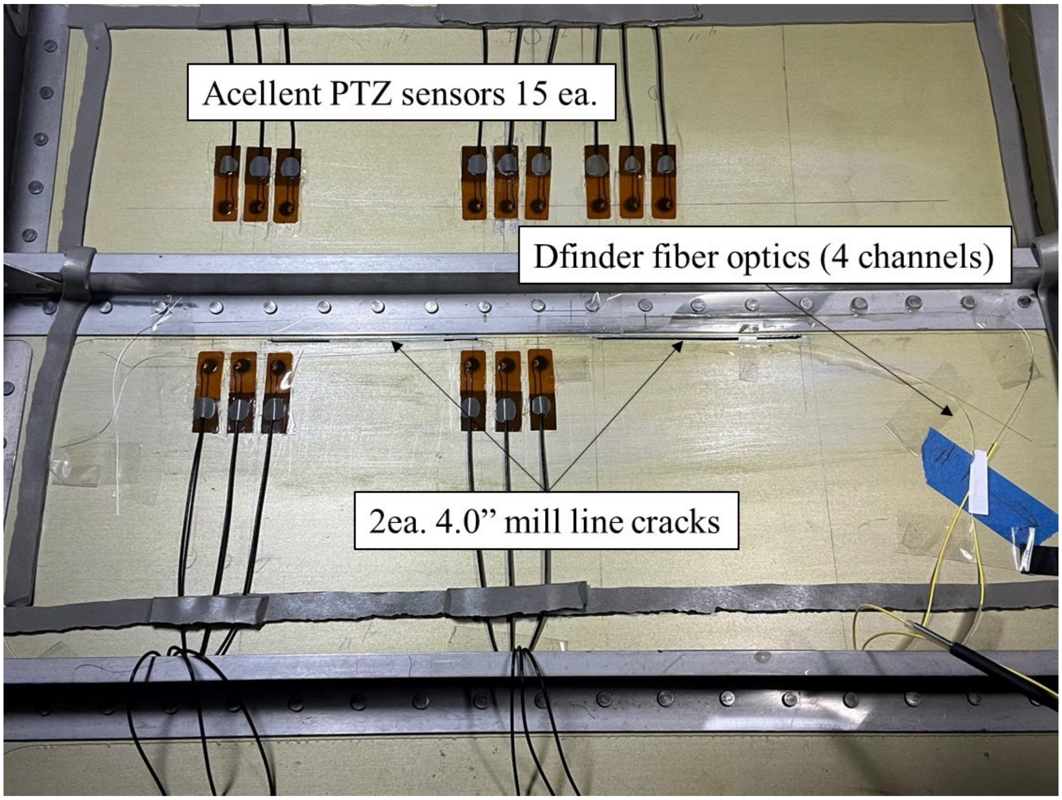

Figure E- 4. HM sensor locations for the second-round mill line crack SHM study

F Frame reinforcement repair

During the Phase 2 fatigue testing, the frame end of F3 was unexpectedly broken at 32,900 cycles even though the panel 3 frame ends were reinforced similar to panel 2. However, it was found that the reinforcement pieces were installed without structural adhesive. The test panel was removed from the FASTER fixture due to the limitation of working space inside of the pressure box and the intensity of the repair work. The broken frame end was reinforced as shown in Figure F- 1. All other frame ends reinforcements were dissembled and reinstalled back with adhesive. The panel was then installed back on the fixture after the repair, and the strain survey was conducted to ensure the fame repair and reinforcements did not change load introduction.

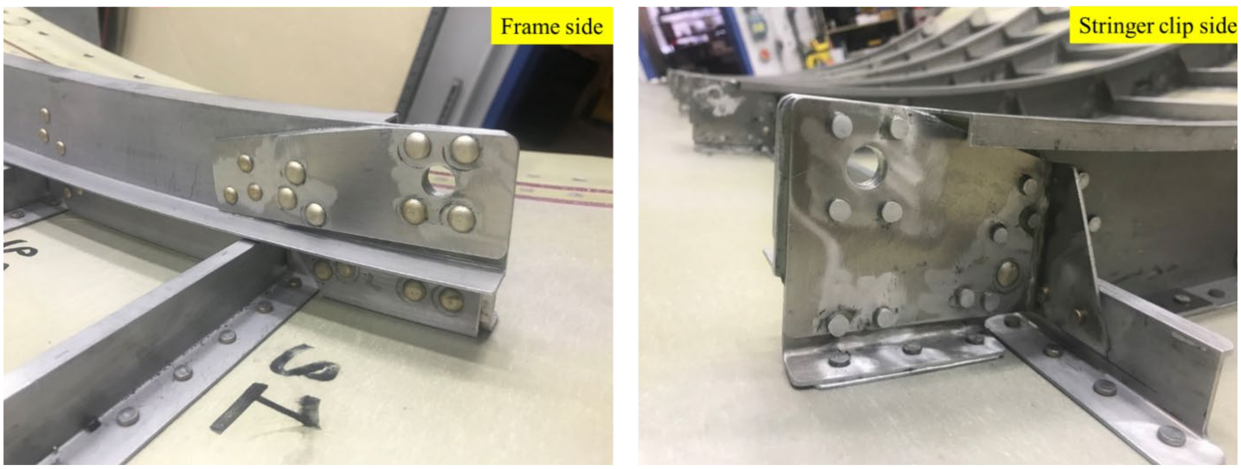

Figure F- 1. Configuration of frame reinforcement repair from both ends

G Residual strength prediction

This appendix presents the analyses for prediction of failure load of Panel 3. Damage scenario is a two-bay longitudinal crack with failed central frame. Finite element model, loading, methodology and results are shown herein.

Finite element model is composed of shell elements (NASTRAN CQUAD4/PSHELL) for skin, stringer and frames, and spring elements for fasteners representation (NASTRAN CBUSH/PBUSH). Mesh size is 5mm for bays near crack, and larger (10/20mm) for the remaining bays.

Damage scenario is a two-bay longitudinal crack with failed central frame, induced in the central stringer bay. Doublers at areas of interface to test rig are not represented, since simplified boundary conditions are employed, and the influence on stresses at central bay is small. Cylindrical quarter-symmetry boundary conditions are applied at side edges.

Furthermore, pressure is applied to skin elements, and axial loads are applied to skin and stringer at forward and rear edges.

Table G- 1 summarizes the finite element model characteristics, as shown in Figure G- 1 to Figure G- 3.

Table G- 1. Panel 3 finite element model characteristics

Characteristic	Description
Skin, stringer, frames	Shell elements (NASTRAN CQUAD4 / PSHELL)
Fasteners	Spring elements (NASTRAN CBUSH / PBUSH)
Longitudinal bays	6 = ½ at fwd panel edge + 5 full bays + ½ at rear panel edge
Frames qty:	6
Transversal bays:	9
Stringers qty:	8
Mesh size at crack area	5mm
Constrains	At lateral edges: ut, θr, θz
Skin stress at fwd/rear edges – Sx:	38.2 MPa
Stringer stress at fwd/rear edges – S,str:	11.85MPa
Pressure load:	8.64psi

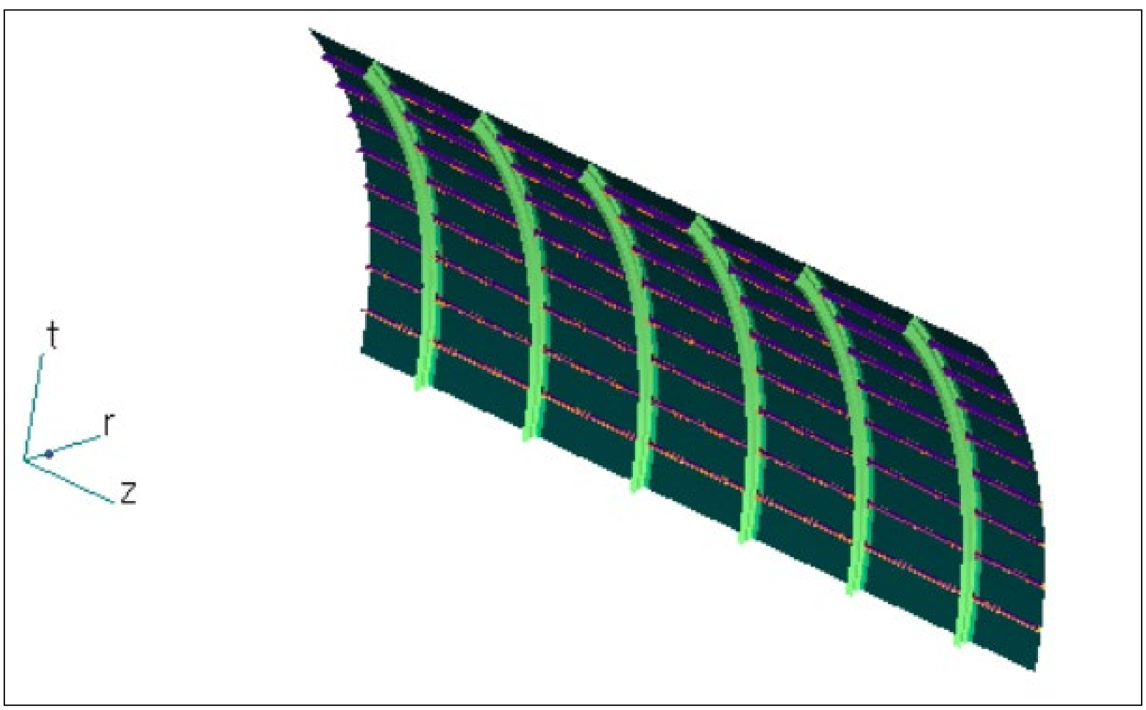

Figure G- 1. Curved panel finite element model – general view and cylindrical coordinate system

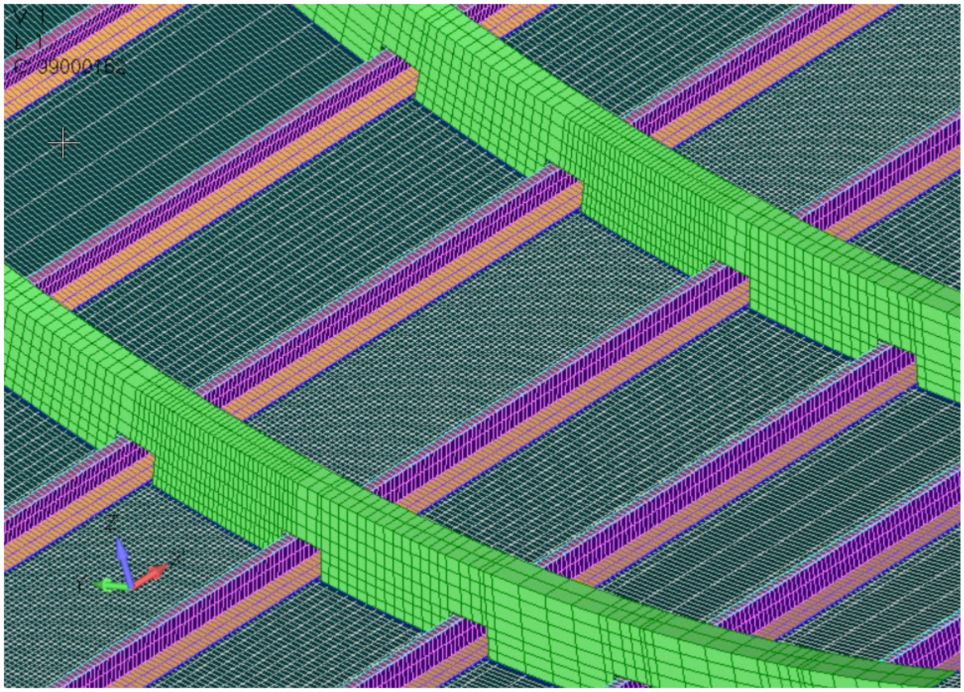

Figure G- 2. Curved panel finite element model – detailed view of skin, stringers and frames

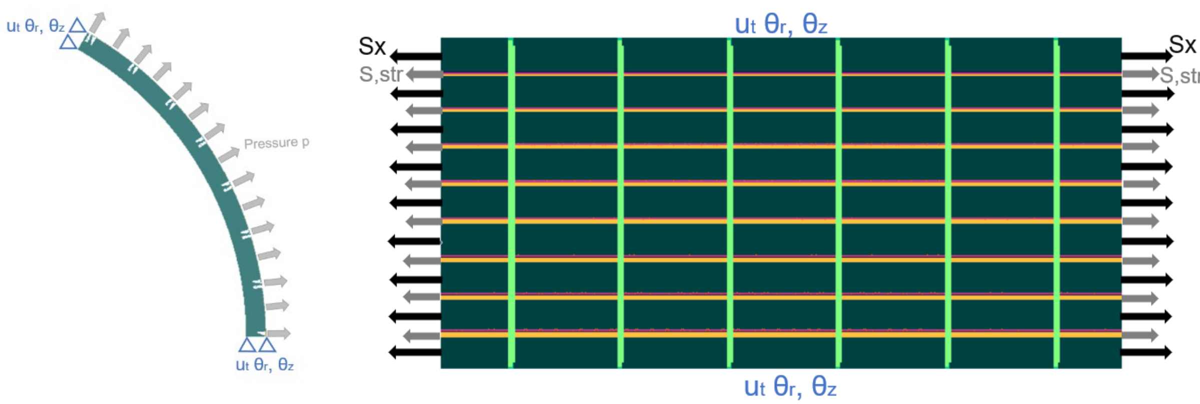

Figure G- 3. Curved Panel boundary conditions – constraints in cylindrical coordinate system, pressure and axial loadings representation

Figure G- 1 presents R-Curves for the Al 2524-T3 and Al 2029-T3 materials, obtained during EMST Project. The comparison of the different materials shows an approximate 8% improvement of Al 2029-T3 compared to Al 2524-T3, in terms of Kr.

Figure G- 5 presents R-Curves for the Al 2524-T3 and Al 2024-T3 materials, granted by Arconic.

Arconic Al 2524-T3 R-Curve (L-T) is modified, by applying an 8% increase on Kr values, for Panel #3 analysis. This curve is applied as alternative to the available Al 2029-T3 curve, due to its longer Δ_{aeff} range.

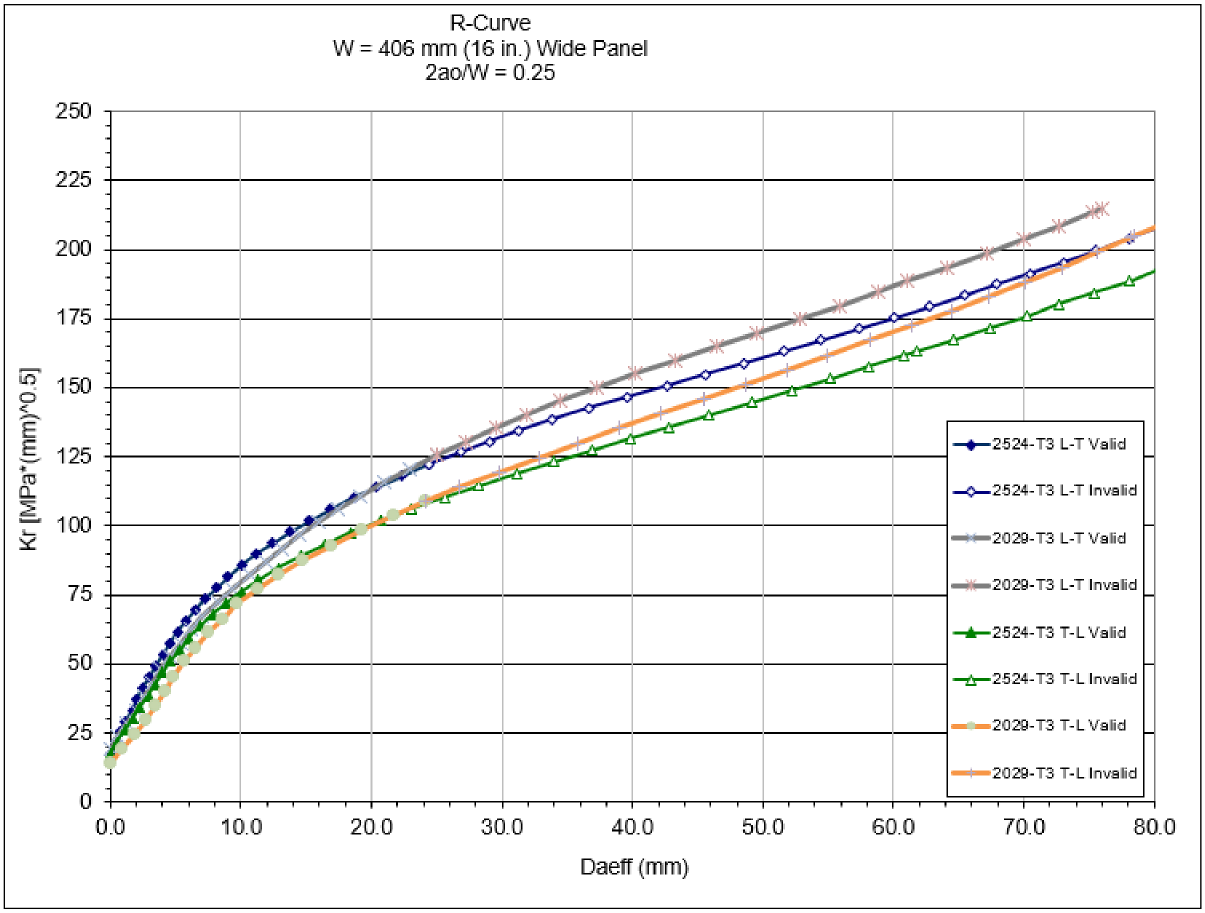

Figure G- 4. Material R-Curves – Al 2524-T3 vs. Al 2029-T3

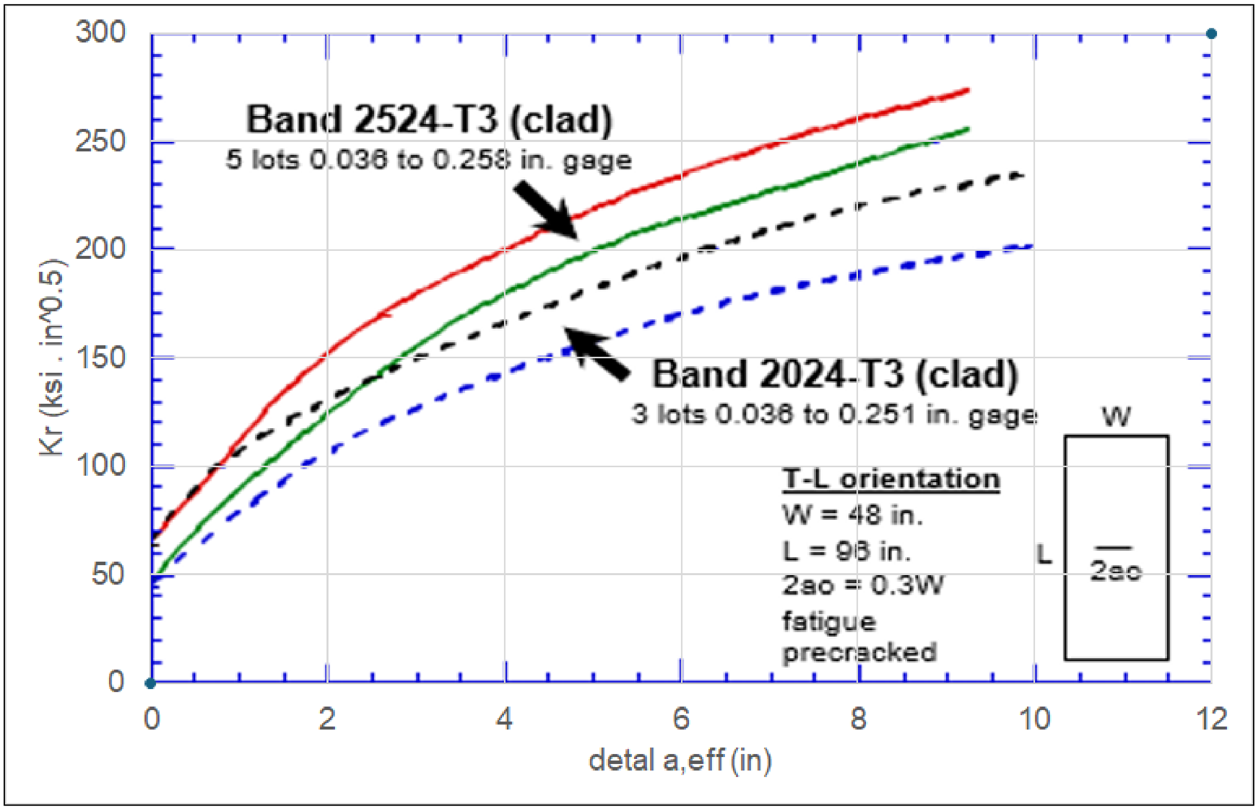

Figure G- 5. Arconic R-Curves – Al 2524-T3 vs. Al 2024-T3 (granted by Arconic)

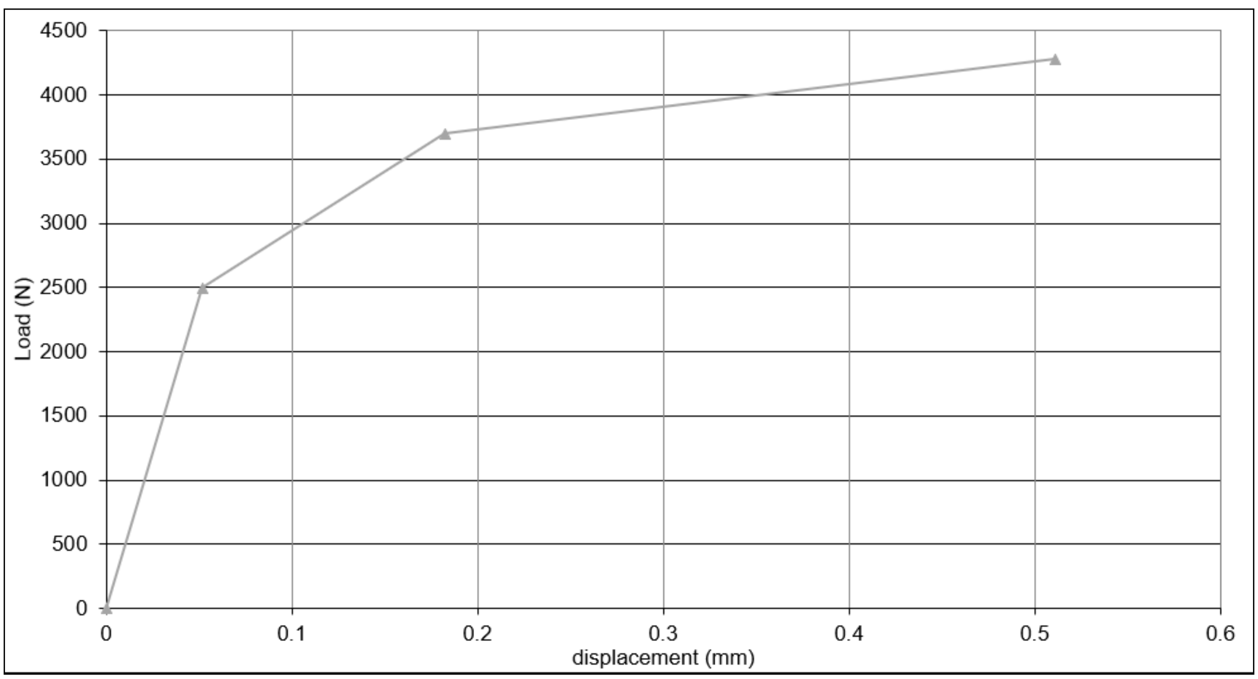

Figure G- 6. Fastener load vs. displacement curve (granted by Arconic)

Stress intensity factors are calculated with the Modified Crack Closure Integral method, as described in (Rahman, Backuckas, Jr., & Bigelow, 2004) .

Crack is simulated by mesh separation, as shown in Figure G- 7 (Rahman, Backuckas, Jr., & Bigelow, 2004).

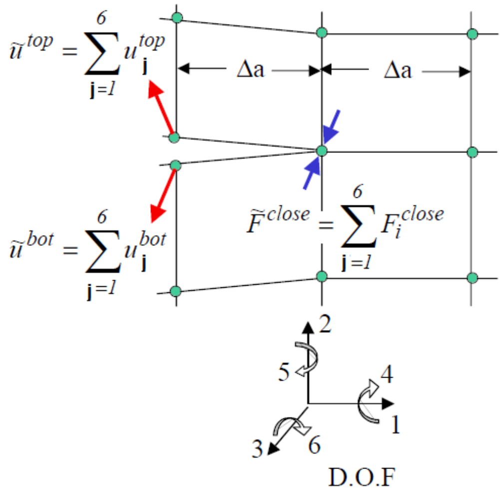

Figure G- 7. Crack tip forces and displacements needed for MCCI Method

In the MCCI method, it is assumed that the energy released during crack extension is equal to the work necessary to close the crack.

The work is calculated using the local crack-tip displacements and forces, from non-linear analysis of each crack step.

The work (Wi) to close a crack in (Δa) for the j_{th} D.O.F is: $W_j = \frac{1}{2t\Delta a}\left[F_j^{close}\left(u_j^{top} - u_j^{bot}\right)\right], j = 1,.2,3,4,5,6$	(1)
The Strain Energy Release Rate - G: $G = \frac{\Delta U}{\Delta A} = W$	(2)
Linear elastic fracture mechanics defines (K) from the Strain Energy Release Rate (G): $G = \frac{K^2}{E}$	(3)
And, for crack propagation Mode I: $\frac{K_I^{\ 2}}{E} = W_2 + W_6$	(4)

Non-linear large displacement analysis solution (NASTRAN Solution 106) is employed for obtaining crack tip forces and displacements for each crack step.

Non-linear fastener load vs. displacement curve is also employed. Skin and frame materials are considered linear elastic since frame does not yield before fastener failure, and skin yielded area ahead crack tip is below linear elastic fracture mechanics limits.

Tearing determination

Tearing length is obtained iteratively, considering acting K curve, and fracture resistance Kr curve or R-curve, according to methodology described in Figure G- 8 (Liu, et al., 2005).

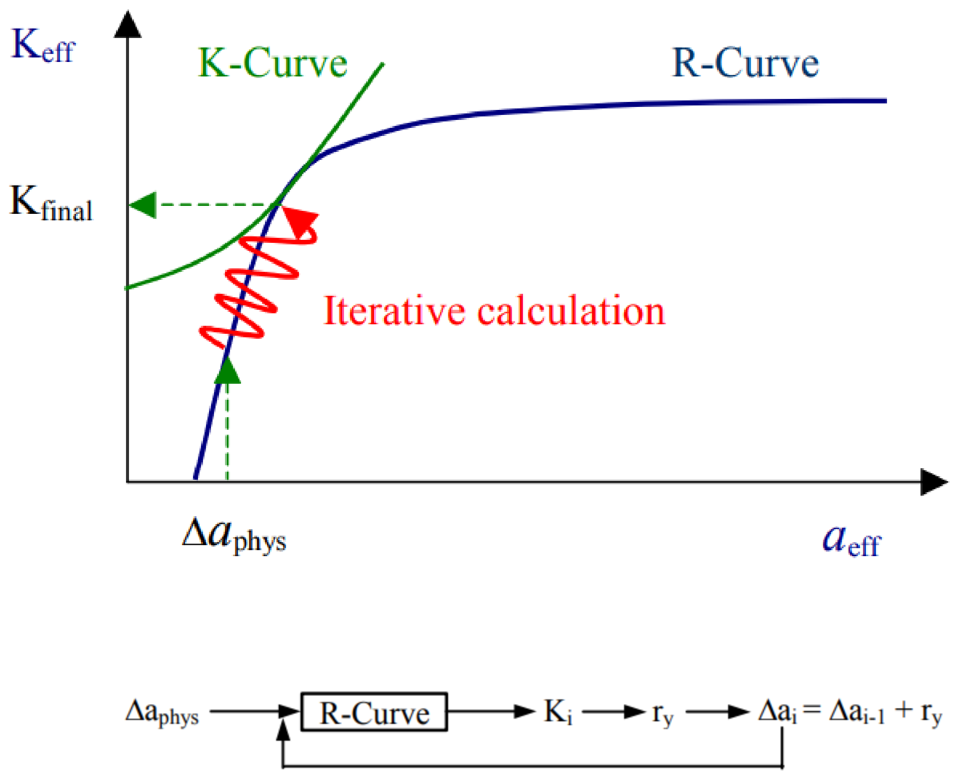

Figure G- 8. Procedure used for the calculation of crack tearing

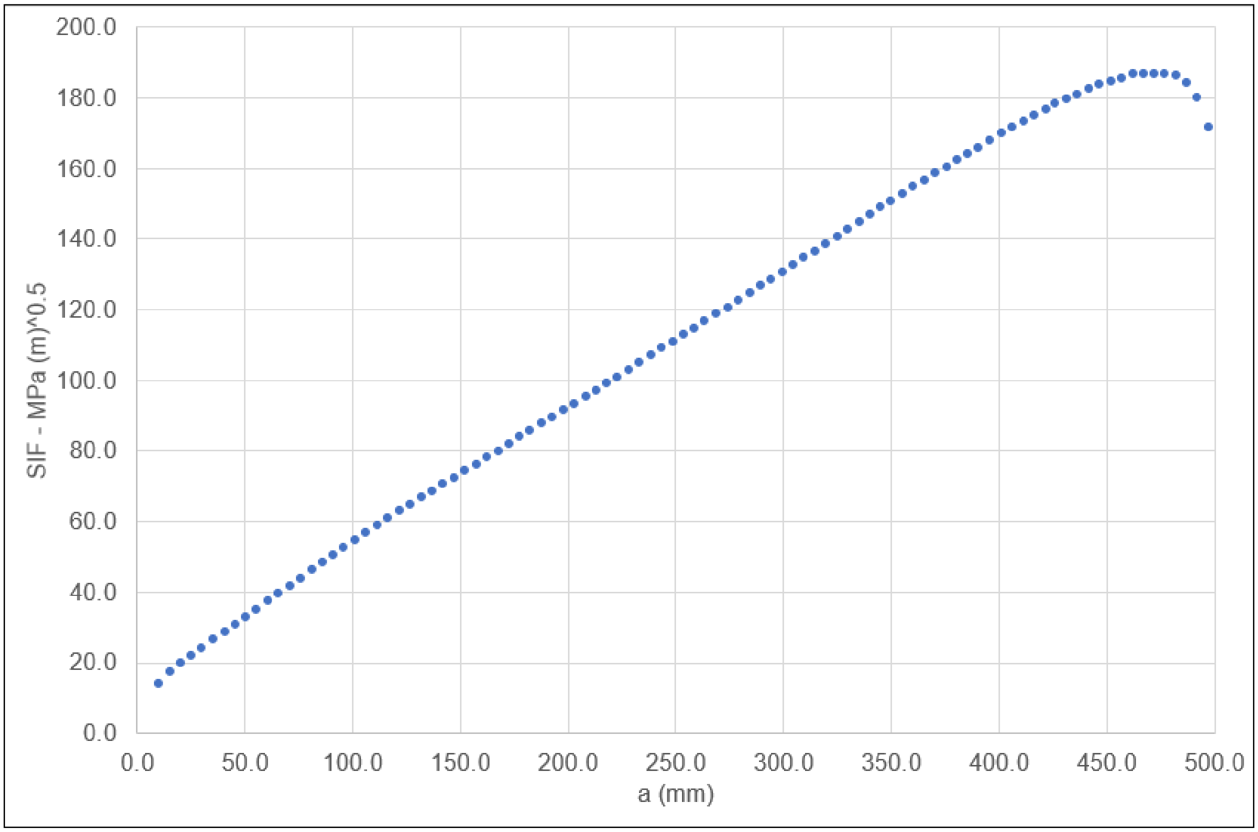

Figure G- 9. Panel #3 – Stress Intensity Factors for pressure 8.64psi – analysis results

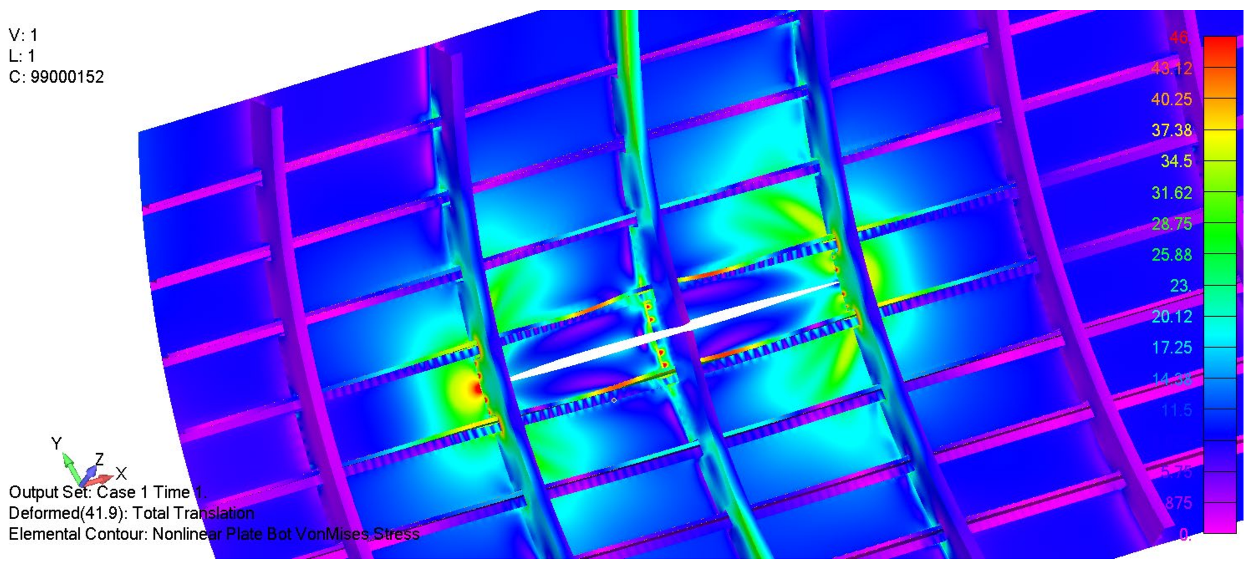

Figure G- 10. Panel #3 – Displacements and Von Mises stresses for pressure 8.64psi – analysis results

Considering that skin material toughness is very large, fastener failure is determining for the overall failure in this panel configuration.

Once fastener load capacity is exceeded, skin crack fracture occurs almost immediately - i.e. very small load increase is supported.

Crack physical crack length, considering initial crack plus tearing, is plotted *vs.* applied pressure load, as shown in Figure G- 10. This curve is valid up to the point either fastener or frame fail.

Fastener residual strength curve and frame residual strength curve are also plotted, in terms of applied pressure. For each crack length, the correspondent pressure load that causes the element failure is considered its residual strength.

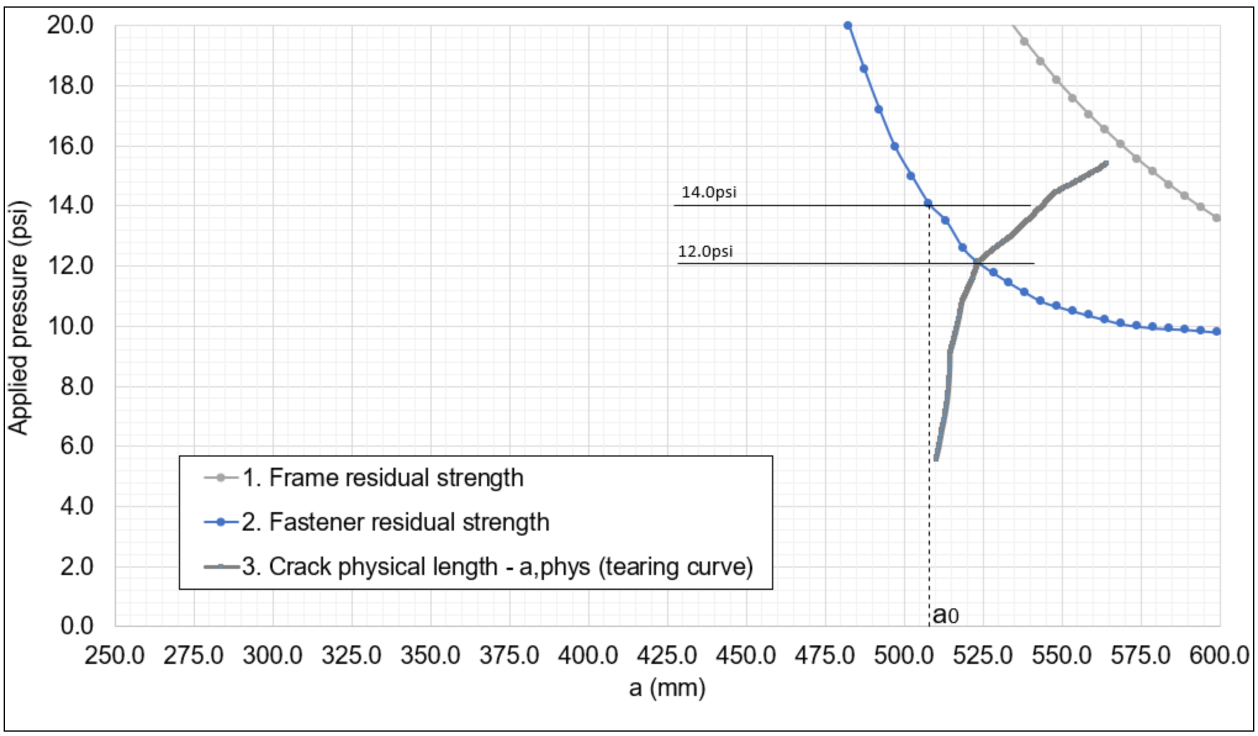

Figure G- 11. Analysis failure prediction

Fastener and frames acting loads increase with the applied pressure and with crack length. The results obtained with 8.64psi are linearized for determination of the residual strength curves of these elements - (curves 1 and 2 from Figure G- 11).

After fastener load capacity is exceeded, due to bearing, crack SIF increases very fast, and therefore the tearing curve is not valid, and no further analysis is performed.

Two panel failure predictions are done – one considering crack tearing, and another one without tearing. This strategy allows to have both upper and lower bounds for the expected failure load.

Predicted failure load – lower bound: 12psi.

Predicted failure load – lower bound: 14psi.

Predicted failure load – average value: 13psi.